**Steel and Composite Structures**, *Vol. 21, No. 4 (2016) 703-753*
DOI: http://dx.doi.org/10.12989/scs.2016.21.4.703


# Evaluation of AF type cyclic plasticity models in ratcheting simulation of pressurized elbow pipes under reversed bending

Xiaohui Chen [*1,2], Bingjun Gao [3] and Xu Chen [2]

[1] *School of Control Engineering, Northeastern University, Qinhuangdao 066004, China*
[2] *School of Chemical Engineering and Technology, Tianjin University, 300072, China*
[3] *School of Chemical Engineering and Technology, Hebei University of Technology, Tianjin, 300000, China*

(*Received February 27, 2016, Revised May 20, 2016, Accepted May 30, 2016*)

**Abstract.** The ratcheting behavior was studied experimentally for Z2CND18.12N elbow piping under cyclic bending and steady internal pressure. Dozens of cyclic plasticity models for structural ratcheting responses simulations were used in the paper. The four models, namely, Bilinear (BKH), Multilinear (MKIN/KINH), Chaboche (CH3), were already available in the ANSYS finite element package. Advanced cyclic plasticity models, such as, modified Chaboche (CH4), Ohno-Wang, modified Ohno-Wang, Abdel Karim-Ohno and modified Abdel Karim-Ohno, were implemented into ANSYS for simulating the experimental responses. Results from the experimental and simulation studies were presented in order to demonstrate the state of structural ratcheting response simulation by these models. None of the models evaluated perform satisfactorily in simulating circumferential strain ratcheting response. Further, improvement in cyclic plasticity modeling and incorporation of material and structural features, like time-dependent, temperature-dependent, non-proportional, dynamic strain aging, residual stresses and anisotropy of materials in the analysis would be essential for advancement of low-cycle fatigue simulations of structures.

**Keywords:** ratcheting strain; cyclic loading; FEA; constitutive model; pressure piping

## 1. Introduction

Ratcheting, one of the stress controlled low cycle fatigue responses, was defined as the accumulation of plastic strain with cycles. In other words, ratcheting, a strain accumulation under stress controlled cycling with non-zero mean stress, was a predominant phenomenon in cyclic plasticity (Gaudin and Feaugas 2004). Ratcheting had also been considered in many design criteria for engineering components and structures, including ASME Code Section III (2007), KTA (1995), EN13445 (2002), R5 (1990) and RCC-MR (1985). The ratcheting behavior of pressurized piping was a typical case in the engineering components and structures. Pressurized piping such as straight pipe, elbows, and even piping systems was widely applied in nuclear, electric, and chemical industries. In addition to fluid pressure, piping components may encounter ratcheting strain under cyclic thermal stress induced from cyclic temperature or under cyclic bending initiated from seismic or the other cyclic loading such as cyclic thermal compression and extension.

*Corresponding author, Ph.D., E-mail: chenxh@neuq.edu.cn


http://www.techno-press.org/?journal=scs&subpage=6 ISSN: 1229-9367 (Print), 1598-6233 (Online)

Generally, the ratcheting response of pressurized elbow was studied experimentally with shaking table and inertia load (Huang *et al*. 1998, Boussaa *et al*. 1993, DeGrassi *et al*. 2003, 2008, Yahiaoui *et al*. 1996a, b). The ratcheting strain of elbow was measured at flank, intrados and extrados. All components failed either by developing a crack at flanks running in the helical direction about the mid-circumference and extending from the mid-meridian between flank and intrados or by a crack at a defect in the weld. The results indicated that fatigue-ratcheting was the major failure mode. Wang *et al*. (2014) investigated experimentally the ratcheting behavior and ratcheting boundary of pressurized straight Z2CND18.12N stainless steel pipe under bending loading and vertical displacement control. The results showed that the cyclic bending loading and the internal pressure affected the ratcheting behavior of the pressurized straight pipe significantly under load control. In the meantime, the ratcheting characteristics were also highly associated with the cyclic displacement and the internal pressure under displacement control. Moreover, the ratcheting boundaries of the pressurized straight Z2CND18.12N stainless steel pipe were determined and compared based on KTA/ASME, RCC-MR and the experimental results. Chen *et al*. (2015, 2016) studied the ratcheting behavior of straight pipe and 90° elbow piping with and without local wall thinning subjected to internal pressure and reversed in-plane bending by means of loading control and displacement control. Hassan and his co-worker (Hassan *et al*. 2015) studied the low-cycle fatigue and ratcheting responses of SS 304L 90 deg long-radius elbows through experimental and analytical studies under displacement-controlled and force-controlled. All elbow specimens tested had failed by axial crack at the flank. Zakavi *et al*. (2014) simulated cyclic loading behavior of carbon steel pressurized piping by means of kinematic hardening model, the piping were subjected to internal pressure and seismic bending. Fenton and Hassan (2014) studied the low-cycle fatigue experiments of short radius elbows which were conducted and force, displacement, and strain data under cyclic loading. The results found the difference fatigue life of short and long radius elbows. Vishnuvardhana *et al*. (2013) studied ratcheting behavior of Type 304LN stainless steel straight pipes and elbows subjected to steady internal pressure and cyclic bending load. The straight pipes failed either by occurrence of through-wall crack accompanied by simultaneous ballooning, or bursting with simultaneous ballooning. All the elbows failed by occurrence of through-wall crack accompanied by simultaneous ballooning. Ratcheting behaviour of straight pipes and elbows were compared and it was generally inferred that ratcheting was more pronounced in straight pipes than in elbows. Varelis *et al*. (2013) investigated the low-cycle fatigue of pipe elbows by means of experiments and determined an accurate numerical model for pipe elbows under severe cyclic in-plane bending, simulating earthquake level loading. Based on the previous experimental work, the numerical models for steel elbow elastic-plastic behavior under cyclic in-plane bending was developed by Varelis and Karamanos (2014). Special attention is given to simulating local strain behavior as well as the constitutive model for describing the material cyclic behavior of steel. The ultimate goal remains to create a simple methodology for reliable fatigue design for steel elbows that fail under low-cycle fatigue. In addition, the ratcheting behavior of pressurized elbow piping was studied experimentally with cyclic quasi-static loading (Chen *et al*. 2005a, 2006, Rahman 2006, Hassan and Rahman 2009, Touboul 1998). On the other hand, finite element analyses were performed for simulating the recorded responses of elbow. The plasticity models considered for finite element analyses are Bilinear (Prager 1956), Multilinear (Besseling 1958) and Chaboche (Chaboche and Dang 1979, Chaboche 1986, 1991) which are currently available in ANSYS. Advanced constitutive models by Bari and Hassan (2002), Ohno-Wang (1993), Chen and Jiao (2004), Chen *et al*. (2005b) and Abdel Karim-Ohno (Abdel-Karim and Ohno 2000) were implemented into ANSYS for improved elbow response simulations.

Ratcheting simulations with ANSYS software were critically evaluated to determine the state of piping component in order to research needed. Chen *et al*. (2013) reviewed the experimental investigation and finite element analysis (FEA) of ratcheting behavior of pressurized piping. Based on experimental and FEA research, ratcheting boundaries have been determined with the final aim of aiding the safety design and assessment of engineering piping structures.

In the present article, Section 2 summarizes the experimental observation of ratcheting behavior of pressurized elbow pipes, which were subjected to the constant internal pressure and cyclic bending loading. In Section 3, the methods of finite element implementation of constitutive models with advanced kinematic hardening rules were briefly introduced. Finite element analyses (FEA) of ratcheting behavior of pressurized elbow piping were evaluated in Section 4. In Section 5, ratcheting boundaries determined by such EPFEA and simplified technique were commented. Finally, the above several sections were concluded.

## 2. Experimental observation

### *2.1 Material and specification of elbow piping*

Experiments were conducted on stainless steel Z2CND18.12N elbow specimens, the chemical compositions of which were listed in Table 1. Fig. 1 gave the geometry of material specimen. The specimen was obtained from the original straight pipes for PWR nuclear power plants along the axial direction, and then were machined into dog-bone type specimens with gage section 10 mm in diameter and gage length of 20 mm in accordance with ASTM standard E606-04.

Tests were carried out on a MTS810 machine, as shown in Fig. 2. All tests were conducted at room temperature. Tensile tests were under stress control (i.e., extensometer control) in sequence.

Table 1 Chemical compositions

| Chemical composition | C | Si | Mn | P | S | Ni | Cr | Mo | B | Cu | Co | N |
|---|---|---|---|---|---|---|---|---|---|---|---|---|
| % | 0.025 | 0.430 | 1.211 | 0.021 | 0.003 | 12.073 | 17.517 | 2.388 | 0.001 | 0.075 | 0.035 | 0.070 |

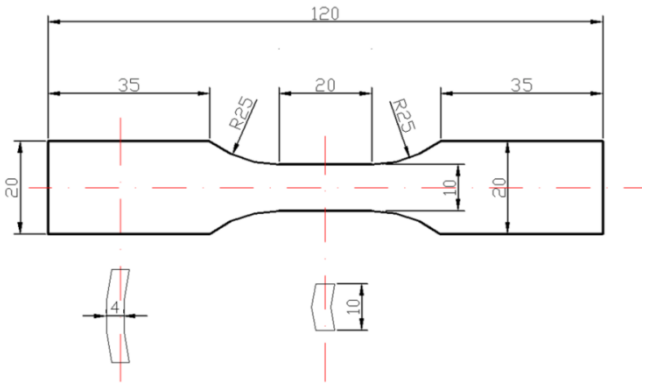


Fig. 1 Geometry of specimen used for tests


(a) (b)

Fig. 2 Equipment: (a) Electro-hydraulic-servo fatigue testing machine; (b) Extensometer

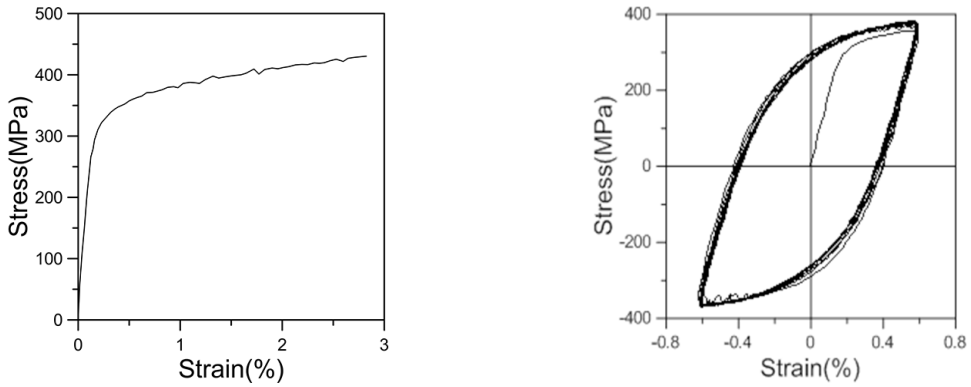


(a) Uniaxial tensile stress-strain curve (b) Stress-strain hysteresis hoop for 100 cycles

Fig. 3 Geometry of specimen used for tests

Extensometer control for the strain rate $1\times10^{-3}$/s ended at the strain of 30% at room temperature, as shown in Fig. 3(a). Cyclic deformation behavior under fully reversed strain cycling can be investigated through the stress-strain hysteresis loop, as shown in Fig. 3(b).

Uniaxial ratcheting experiments were conducted under the same stress rate, in order to study the effect of mean stress and stress amplitude on ratcheting behavior of Z2CND18.12N stainless steel, as shown in Fig. 4. It was seen from Figs. 4(a) and 5(a) that the loading period in the first cycle was repeated under different mean stress or stress amplitude. Results indicated that the relationship between stress and strain was steady for uniaxial ratcheting tests. Initial stress-strain hysteresis loop of 200 MPa was more obvious than that of 150 MPa. Figs. 4(b) and 5(b) gave the evolution between ratcheting strain and number of cycles. Results observed that ratcheting strain was rapid accumulation in the initial cycles and smooth and steady increasing in subsequent cycles, namely progressive ratcheting strain occurred and ratcheting strain rate was constant. Ratcheting strain increased with the increasing of mean stress/ stress amplitude under the constant stress amplitude/mean stress.

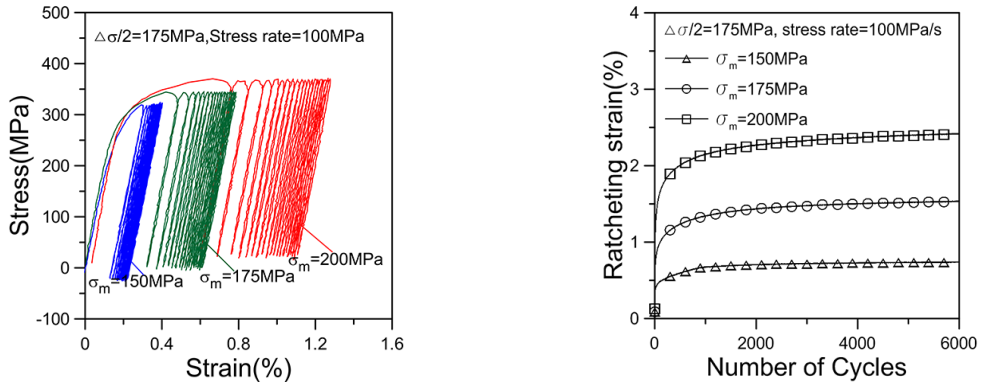


(a) (b)

Fig. 4 Uniaxial ratcheting tests with the constant amplitude of 150 MPa and different mean stresses (a) stress-strain curve (the first 20 cycles); and (b) ratcheting strain evolution

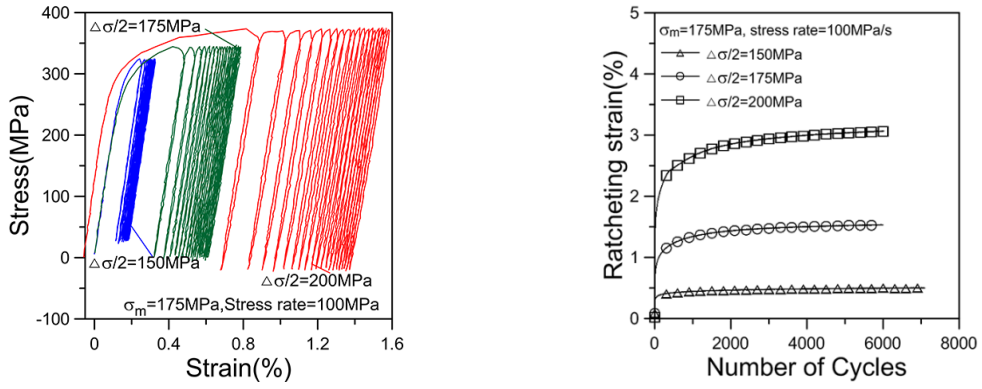


(a) (b)

Fig. 5 Uniaxial ratcheting tests with the constant stress amplitude of 200 MPa and different mean stresses: (a) stress-strain curve (the first 20 cycles); and (b) ratcheting strain evolution

### *2.2 Experimental apparatus and testing system*

Experimental apparatus was shown in Fig. 6. The elbow samples met Chinese National Standard GB12459-90. The specimens were constructed of 76 mm diameter, 4.5 mm in nominal thickness, 90 degree, long radius (mean bend radius 95 mm) elbow pipe, each of which was butt welded to a 100 mm long straight pipe.

The connecting blocks were screwed into the pipe ends of the elbow piping, and loading bars were connected with the connecting blocks through pins. The loading bars were clipped in the clip head of the multi-axial test machine, as shown in Fig. 7. Inner pressure was applied via pressurized hydraulic oil through the lower lug using pressurized system in experiments. The upper loading bar was pin connected to the actuator rod that applied displacement or force controlled loading to the elbow specimen. Cyclic pull-push of the test machine opened and closed the elbow and in effect bends the specimen reversely.

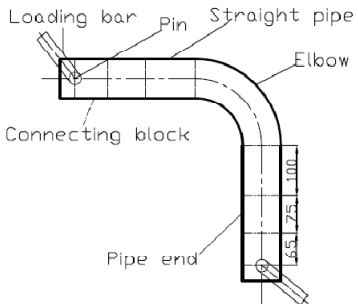


Fig. 6 Sketch of specimen

Fig. 7 Setup of experiment apparatus

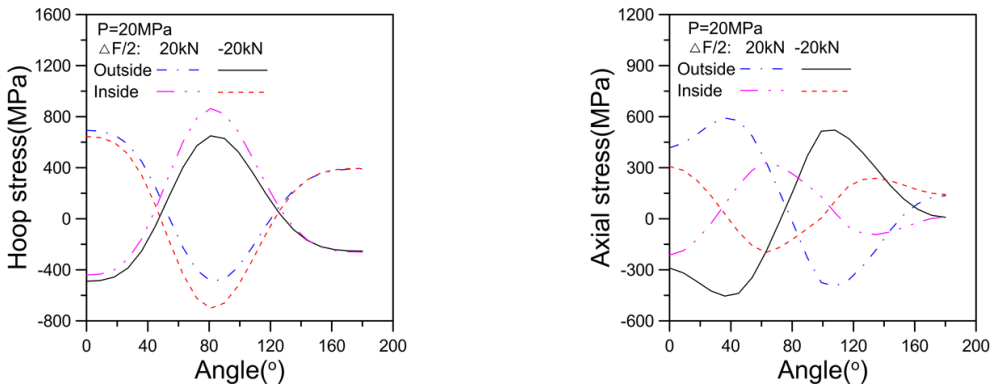


(a) (b)

Fig. 8 Elastic nominal stress distribution: (a) hoop stress; (b) axial stress

### *2.3 Strain gauge location pattern*

Moreton *et al*. (1996) simulated the stress distribution of pressurized long radius elbow under in-plane bending by elastic finite element analysis. It was shown that the most likely suffering ratcheting strain could occur at flanks and midway between intrados and flanks. In this paper, the

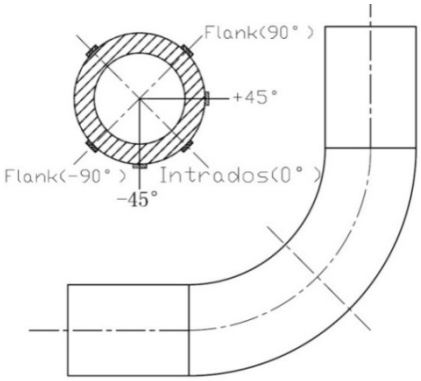


Fig. 9 Gauges distribution

Table 2 Test conditions

| Spec. no. | Loading step | Inner pressure (MPa) | Bending load (kN) | Number of cycles | Cycle time (s) |
|---|---|---|---|---|---|
| 12SER1 | 1 | 17.5 | 20 | 55 | 30 |
| | 2 | 20 | 20 | 30 | 30 |
| | 3 | 17.5 | 20 | 20 | 30 |
| 12SER2 | 1 | 20 | 20 | 13 | 30 |
| 12SER3 | 1 | 10 | 20 | 200 | 30 |
| | 2 | 15 | 20 | 20 | 30 |
| | 3 | 10 | 20 | 20 | 30 |
| | 4 | 20 | 20 | 20 | 30 |
| 12SER4 | 1 | 17.5 | 15 | 150 | 30 |

elastic stress distributions of elbow pipe under inner pressure of 20 MPa and a bending loading of 20 kN was shown in Fig. 8. It was observed that the elastic stress distribution of elbow pipe was the same as that of Moreton's. Thus, the strain gauges were distributed as the pattern in Fig. 9. The strain gauges used were all biaxial strain gages, and thus both axial and circumferential strains were measured at intrados (0°), 45° position at midway between flank and intrados, both flanks (90°) and extrados (180°).

### *2.4 Experimental results and analysis*

The experiments were carried out on elbow pipe with Z2CND18.12N austenitic stainless steel. The loadings prescribed to the four tests were shown in Table 2.

#### *2.4.1 Ratcheting behavior of 90° elbow pipe under a bending loading with constant inner pressure*

Fig. 10 gave loading spectrum in elbow specimen 12SER1 experiment. The pressure fluctuation was very small, as shown in Fig. 10(a). Therefore, the influence of pressure fluctuation on ratcheting deformation can be neglected. Fig. 10(b) showed the relationship between time and bending loading, namely, triangular wave loading control was applied in the paper.

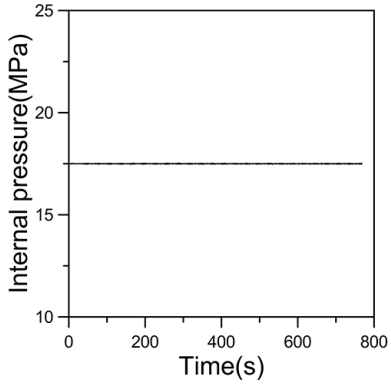


(a) Internal pressure versus time

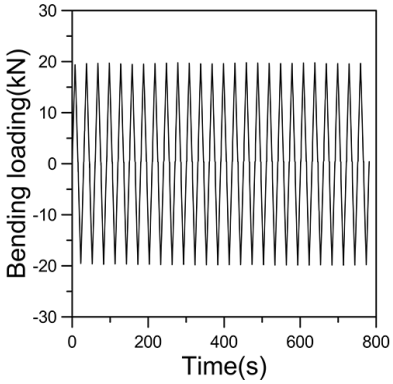


(b) Bending loading versus time

Fig. 10 Loading spectrum

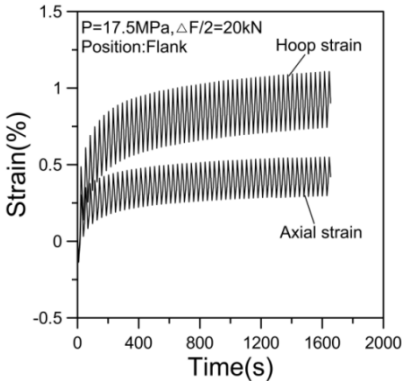


(a) At flank

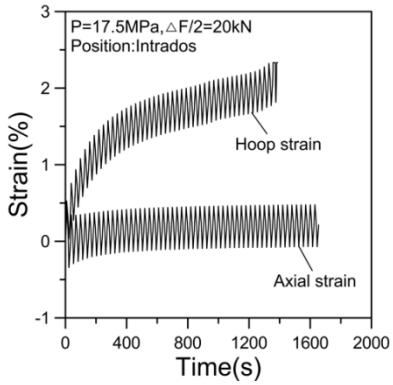


(b) At intrados

Fig. 11 Strain history

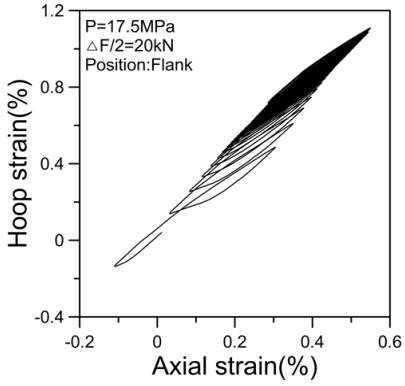


(a) At flank

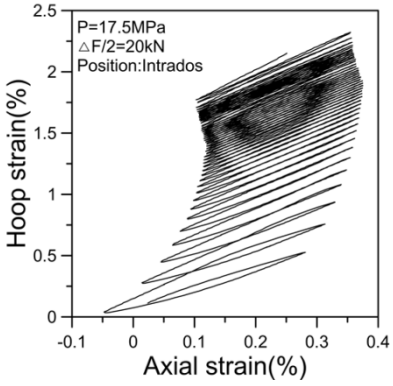


(b) At intrados

Fig. 12 Relationship between hoop strain and axial strain

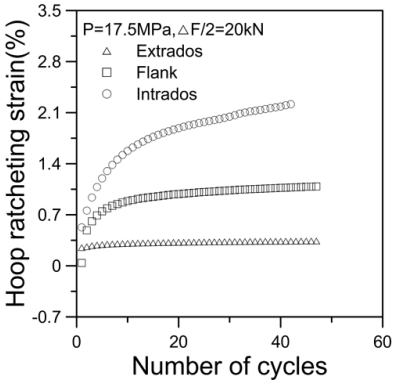


(a) At flank

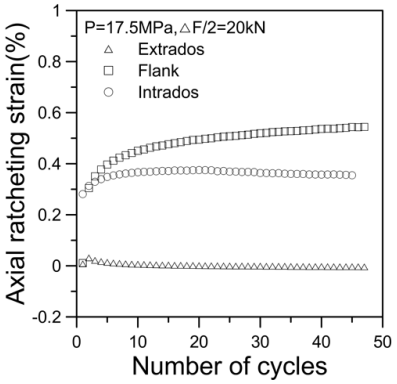


(b) At intrados

Fig. 13 Axial and hoop strain responses of elbow piping

Fig. 14 Cut cross section of an elbow piping

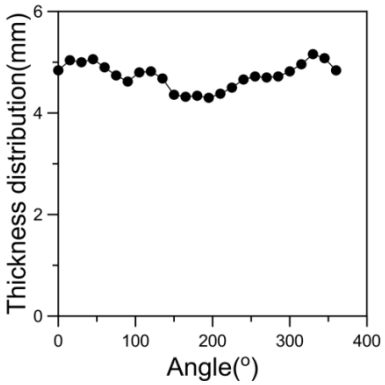


Fig. 15 The thickness of elbow piping

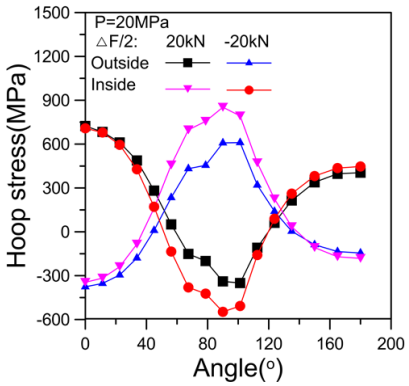


(a) Hoop stress

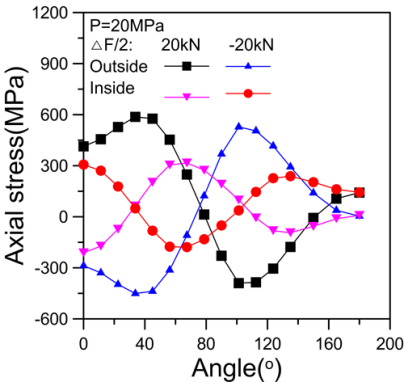


(b) Axial stress

Fig. 16 Elastic nominal stress distribution of elbow with real thickness

The curves of hoop strain and axial strain versus time at flank and intrados were respectively given in Figs. 11(a)~(b) for the specimen 12SER1. Figs. 12(a)~(b) indicated the relationship between axial strain and hoop strain at flank and intrados, respectively. It was found that the bigger ratcheting strain occurred at flank and intrados. The maximum ratcheting strain occurred at the hoop direction. Hoop ratcheting strain decreased with the increasing the number of cycles, but shakedown did not appear.

Fig. 13 showed a comparison of ratcheting strain in the long radius 90° elbow under inner pressure of 17.5 MPa and bending loads of 20 kN. The axial and hoop ratcheting strains of the elbow occured at flanks, intrados and extrados, as shown in Figs. 13(a)~(b). It was shown that ratcheting strain occured mainly in the circumferential directions of the elbow. The hoop ratcheting strain at intrados was larger than those of the flank in this experiment. The ratcheting strain was calculated from the strain history by maximum method, namely the maximum strains of each cycle.

The maximum ratcheting strains were not all occurred at intrados for the specimens, which were largely attributed to the processing of elbow pipe with non-homogeneous wall thickness (Chen *et al*. 2006). Fig. 14 gave the cut cross section of elbow piping. The intrados (0°) thickness was 4.84 mm, flank (90°) thickness 4.62 mm and extrados (180°) thickness 4.34 mm. However, the thinnest position was about 10 degree away from the extrados (180°) with a thickness of 4.3 mm, while the nominal thickness was 4.5 mm, as shown in Fig. 15. Elastic nominal stress distribution of elbow with real thickness was shown in Figs. 16(a)~(b). Compared with Fig. 8, it was found that hoop stress distribution in Fig. 16(a) was larger fluctuated than that in Fig. 8. Theoretically, maximum ratcheting strain should occured at flanks and no ratcheting strain was found at the extrados for all tests. However, in reality, maximum ratcheting strains occured sometimes at intrados, which was attributed to that the elbow was usually losing thickness at the extrados and gaining at the intrados. Standard elbows generally specified the thickness, losing no more than 12.5%, thickness gaining was not specified, but up to 25% may occur for standard long radius elbows. The thicker wall of elbow pipe at intrados had the less ratcheting strain (Chen *et al*. 2006). Thus, only ratcheting strains at flanks (90°) were compared below.

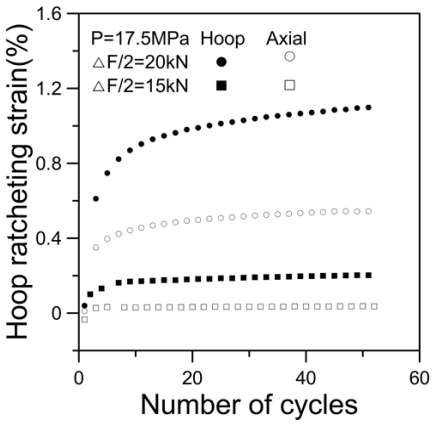


Fig. 17 Comparison of ratcheting strain under inner pressure of 17.5 MPa and bending loadings of 15 kN and 20 kN

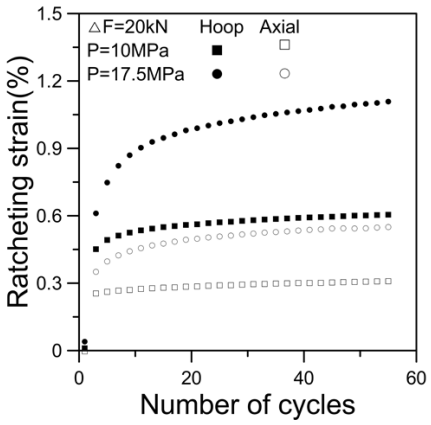


Fig. 18 Ratcheting strain (ΔF/2 = 20 kN, P = 10 MPa and 17.5 MPa)

### *2.4.2 Ratcheting behavior of 90° elbow pipe under different bending loadings with the same constant inner pressure*

Fig. 17 showed a comparison of ratcheting strain for elbow pipe under inner pressure of 17.5 MPa and bending loadings of 15 kN and 20 kN. It was shown that the ratcheting strain rate increased with a bending loading under the same inner pressure, and the hoop ratcheting strain was larger than that of axial direction.

### *2.4.3 Ratcheting behavior of 90° elbow pipe under different internal pressures and the same bending loading*

Axial and hoop ratcheting strains were given in Fig. 18 for tests of 20 kN bending loading under various inner pressures (10 MPa and 17.5 MPa) from individual specimens. It was observed that the ratcheting strain rate increased with inner pressure under the same bending loading, and hoop ratcheting strains was larger than those of axial directions.

### *2.4.4 Ratcheting behavior of 90° elbow pipe under same constant inner pressure and multi-step bending loadings*

Fig. 19(a) showed the ratcheting strain of a specimen with a bending loading of 20 kN and multi-step bending loadings of 17.5 MPa, 20 MPa and 17.5 MPa (first step 55 cycles, second step 30 cycles, third step 20 cycles). Hoop and axial ratcheting strains at flank were given in Fig. 19(b) for a specimen with a bending loading 20 kN and multi-step inner pressures of 10 MPa, 15 MPa, 10 MPa and 20 MPa (first step 200 cycles, second step 20 cycles, third step 20 cycles, fourth step 20 cycles). It was notable that hoop ratcheting strain and hoop ratcheting strain rate rised significantly with inner pressure under constant bending loading. However, the axial ratcheting strain varied much less. It was found that the hoop ratcheting strain rate decreased significantly or even vanishes when a lower inner pressure was applied after a higher level of inner pressure. The main reason was that the decrease of plastic strain is attributed to the shift of yield surface due to the higher inner pressure (Gao *et al*. 2006).

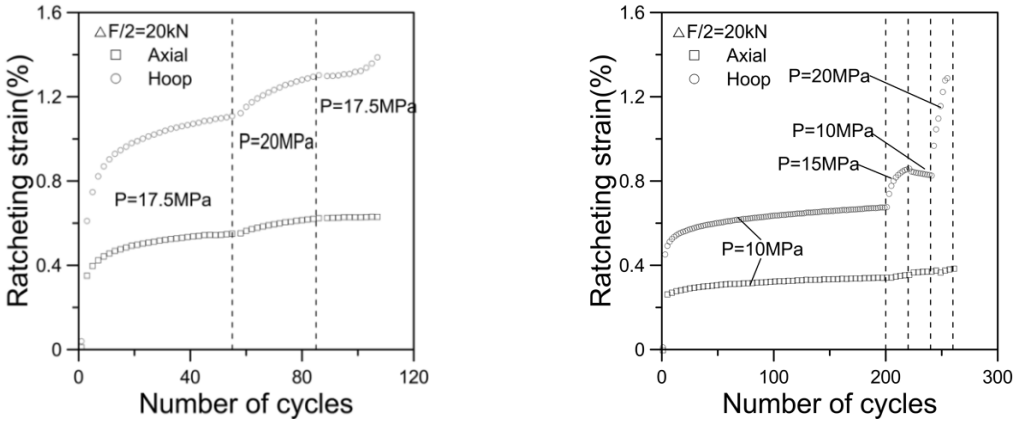


Fig. 19 Ratcheting strain versus number of cycles: (a) P = 17.5, 20 and 17.5 MPa, ΔF/2 = 20 kN); (b) P = 10, 15, 10 and 20 MPa, ΔF/2 = 20 kN)

## 3. Cyclic plasticity constitutive models

### 3.1 BKH model

BKH model was first proposed by Prager (1956) which was the simple linear form of kinematic hardening rule.

$$d\boldsymbol{\alpha}=Cd\boldsymbol{\varepsilon}_p \tag{1}$$

BKIN model assumed that the total stress range was equal to twice the yield stress, so that the Bauschinger effect was included. BKIN model may be used for materials that obey von Mises yield criteria (which includes most metals). The material behavior was described by a bilinear total stress-total strain curve starting at the origin and with positive stress and strain values. The initial slope of the curve was taken as the elastic modulus of the material. At the specified yield stress (C1), the curve continued along the second slope defined by the tangent modulus, C2 (having the same units as the elastic modulus). The tangent modulus cannot be less than zero nor greater than the elastic modulus. With this plasticity model material stress-strain was represented by a linear elastic and a linear plastic part. For uniaxial loading, the kinematic hardening rule dictated the linear movement of the yield surface in stress-plastic strain space. The simplicity linearity of the model allowed fast calculation for finite element simulation. Aslo, the model had the advantage of having only one plasticity parameter C which can be easily determined from a uniaxial stress-strain response. Bari and Hassan (2000) demonstrated that the the Bilinear plasticity model (Prager 1956) fails to produce ratcheting under cyclic loading and elastic shakedown phenomena. As this model was widely used, its performance in simulating ratcheting responsed of piping components would be evaluted in this study.

### 3.2 MKIN model/KINH model

Besseling (1958) and Owen *et al*. (1974) proposed respectively the multilinear kinematic model which was also as sublayer or overlay model. The uniaxial stress-strain curve was represented by several linear segments. The stress $\sigma$ of uniaxial loading condition was calculated from strain $\varepsilon$ (for $\varepsilon > \varepsilon_3$).

$$\sigma = E\left[t_1\varepsilon_1 + t_2\varepsilon_2 + t_3\varepsilon_3 + t_4\varepsilon\right] \tag{2}$$

where $t_1 = \dfrac{E - E_{T1}}{E}$, $t_2 = \dfrac{E_{T1} - E_{T2}}{E}$, $t_3 = \dfrac{E_{T2} - E_{T3}}{E}$, $t_4 = \dfrac{E_{T3}}{E}$.

The smooth shape of stress-strain curve can be simulated by the MKIN/KINH model when the number of linear segments was more than enough. The plasticity model parameters in finite element package ANSYS can be calculated from the stress-strain point. The MKIN/KINH model was popular for analysis with ANSYS due to easy parameters determination for the plasticity model. There was a disadvantage of this plasticity model that failed to predict ratcheting behavior under uniaxial loading and underpredicts ratcheting strain under multiaxial loading.

### 3.3 Armstrong-Frederic model

Armstrong and Frederic (1966) first proposed a non-linear kinematic hardening model that considered strain hardening and dynamic recovery (called as AF model hereafter). Dynamic recovery incorporated the fading memory effect of the strain path and essentially made the rule

nonlinear in nature which was driven by the accumulated plastic strain rate $\dot{p}$. The kinematic hardening rule in this model was given in the form.

$$d\boldsymbol{\alpha}=\frac{2}{3}Cd\boldsymbol{\varepsilon}_p-\gamma\boldsymbol{\alpha}dp \tag{3}$$

where $dp=\sqrt{2/3\left(d\boldsymbol{\varepsilon}_p:d\boldsymbol{\varepsilon}_p\right)}$. For uniaxial loading, the Eq. (3) reduced to the following form

$$\boldsymbol{\alpha}_x=\frac{C}{\gamma}\left[1-\exp(-\gamma\varepsilon_x^p)\right] \tag{4}$$

The Eq. (4) represented the translation of the yield surface. For a cyclically stable material, the uniaxial stress path was obtained by simply adding to $\alpha_x$ the yield surface size $\sigma_0$. For small strain ranges, the AF model can give the nonlinear part of the stress-strain response reasonably well. For large strain ranges, the constant stress was kept. Therefore, the AF model overpredicted the uniaxial ratcheting strain rate.

### *3.4 Chaboche model*

Three or more AF kinematic hardening rules were superimposed by Chaboche and his co-workers (Chaboche and Dang 1979, Chaboche 1986) in the following form

$$\boldsymbol{\alpha}=\sum_{i=1}^{M}\boldsymbol{\alpha}_i,\qquad d\boldsymbol{\alpha}_i=\frac{2}{3}C_i d\boldsymbol{\varepsilon}_p-\gamma_i\boldsymbol{\alpha}_i dp \tag{5}$$

Each of the Chaboche kinematic hardening rule (called as CH3 model hereafter) had its specific purpose. The first rule $\alpha_1$ represented the initial nonlinear part and starts hardening with a very large modulus and stabilized very quickly. The second rule $\alpha_2$ should simulate the transient nonlinear portion of the stable hysteresis curve. The third rule $\alpha_3$ should be a linear hardening rule to represent the subsequent linear part of the hysteresis curve at a high strain range. Therefore, Comparison of CH3 model and AF model improved the uniaxial ratcheting strain. But the CH3 model overpredicted the uniaxial ratcheting strain.

Chaboche (1991) proposed that the four decomposed rule is introduced into CH3 model in order to further improve ratcheting simulation (called as CH4 model hereafter). The kinematic hardening rule in this model was given in the following form.

$$d\boldsymbol{\alpha}_4=\frac{2}{3}C_4 d\boldsymbol{\varepsilon}_p-\gamma_4\boldsymbol{\alpha}_i dp\left\langle 1-\frac{\overline{\boldsymbol{\alpha}_4}}{f\left(\boldsymbol{\alpha}_4\right)}\right\rangle \tag{6}$$

where $\overline{\alpha}_4$ was called the threshold term. Bari and Hassan (2000) observed that CH4 model can simulate the stress-strain curve and uniaxial ratcheting strain well. But it still overpredicted multiaxial ratcheting response.

### *3.5 Ohno-Wang and modified Ohno-Wang models*

#### *3.5.1 OW I model*

Ohno and Wang (1993a) initially proposed a superposition of several kinematic hardening rules

(called as OW I model hereafter). The OW I model used the term $\left\langle d\boldsymbol{\varepsilon}_p : \frac{\boldsymbol{\alpha}_i}{\boldsymbol{\alpha}_i} \right\rangle$ in place of *dp* in the AF model, CH3 model and CH4 model. The kinematic hardening rule in this model was given in the form.

$$\boldsymbol{\alpha}=\sum_{i=1}^{M}\boldsymbol{\alpha}_i, \quad d\boldsymbol{\alpha}_i=\frac{2}{3}C_i d\boldsymbol{\varepsilon}_p-\gamma_i H\left(f_i\right)\left\langle d\boldsymbol{\varepsilon}_p : \frac{\boldsymbol{\alpha}_i}{\boldsymbol{\alpha}_i}\right\rangle\boldsymbol{\alpha}_i \tag{7}$$

For a uniaxial case, the OW I model became a multilinear model. The multilinear models cannot produce uniaxial ratcheting strain due to the prediction of closed hysteresis loops.

### 3.5.2 OW II model

To avoid the limitation of the OW I model, a slight nonlinearity was used by replacing the Heaviside step function by Ohno and Wang (1993b) (called as OW II model hereafter). The kinematic hardening rule in this model was given in the form.

$$\boldsymbol{\alpha}=\sum_{i=1}^{M}\boldsymbol{\alpha}_i, \quad d\boldsymbol{\alpha}_i=\frac{2}{3}C_i d\boldsymbol{\varepsilon}_p-\gamma_i\left(\frac{\overline{\boldsymbol{\alpha}_i}}{r_i}\right)^{m_i}\left\langle d\boldsymbol{\varepsilon}_p : \frac{\boldsymbol{\alpha}_i}{\boldsymbol{\alpha}_i}\right\rangle\boldsymbol{\alpha}_i \tag{8}$$

The slight nonlinearities of the OW II model prevented stress-controlled hysteresis loops from closing and produce uniaxial ratcheting behavior. For a uniaxial case, the term $\left\langle d\boldsymbol{\varepsilon}_p : \frac{\boldsymbol{\alpha}_i}{\boldsymbol{\alpha}_i} \right\rangle$ was similar to *dp*. For a multiaxial case, they produced different directions of kinematic hardening and OW II model improves the ratcheting simulation. The OW II model simulated the stress-controlled ratcheting hysteresis loop more closely than the CH3 and CH4 model, which was not only attributed to the effect of the term $\left\langle d\boldsymbol{\varepsilon}_p : \frac{\boldsymbol{\alpha}_i}{\boldsymbol{\alpha}_i} \right\rangle$, but also the effect of the slight nonlinearities and with the multiplier with power of $m_i$. The parameter $m_i$ affected ratcheting simulation.

### 3.5.3 Mc model

OW II model can simulate uniaxial ratcheting strain reasonably well although it still overpredicted multiaxial ratcheting response. Therefore, McDowell (1995, 1997) modified the OW II model because the parameter $m_i$ was not compatible for a uniaxial case and multiaxial case (called as MD model hereafter).

$$\boldsymbol{\alpha}=\sum_{i=1}^{M}\boldsymbol{\alpha}_i, \quad d\boldsymbol{\alpha}_i=\frac{2}{3}C_i d\boldsymbol{\varepsilon}_p-\gamma_i\left(\frac{\overline{\boldsymbol{\alpha}_i}}{r_i}\right)^{m_i}\left\langle d\boldsymbol{\varepsilon}_p : \frac{\boldsymbol{\alpha}_i}{\boldsymbol{\alpha}_i}\right\rangle\boldsymbol{\alpha}_i \tag{9}$$

where, $m_i = A_i\left\langle \mathbf{n}' : \frac{\boldsymbol{\alpha}_i}{\boldsymbol{\alpha}_i}\right\rangle^{B_i}$, $\mathbf{n}' = \frac{d\boldsymbol{\varepsilon}_p}{dp} = \frac{3}{2\sigma_0}\left(\mathbf{s}-\boldsymbol{\alpha}\right)$.

### 3.5.4 JS and MJS model

Jiang and Sehitoglu (1996) observed that the multiaixal ratcheting parameter was not contained

in the AF model, Chaboche model, Ohno-Wang model. These models cannot simulate uniaxial ratcheting strain reasonably well. Therefore, Jiang and Sehitoglu initially modified the OW II model which was listed in the following (called as JS model hereafter)

$$\boldsymbol{\alpha}=\sum_{i=1}^{M}\boldsymbol{\alpha}_i, \qquad d\boldsymbol{\alpha}_i=\frac{2}{3}C_i d\boldsymbol{\varepsilon}_p-\gamma_i\left(\frac{\overline{\boldsymbol{\alpha}_i}}{r_i}\right)^{m_i}\boldsymbol{\alpha}_i dp \tag{10}$$

$$m_i = A_{0i}\left\langle 2-\mathbf{n}' : \frac{\boldsymbol{\alpha}_i}{\overline{\boldsymbol{\alpha}_i}}\right\rangle^{B_i} \tag{11}$$

where $\mathbf{n}' = \dfrac{d\boldsymbol{\varepsilon}_p}{dp} = \dfrac{3}{2\sigma_0}(\mathbf{s}-\boldsymbol{\alpha})$.

It was shown from Eq. (10) that the term $\left\langle d\boldsymbol{\varepsilon}_p : \dfrac{\boldsymbol{\alpha}_i}{\overline{\boldsymbol{\alpha}_i}}\right\rangle$ in the OW II model was replaced by the term $dp$ in the AF model and the evolution function of the parameter $m_i$ was shown in Equation (11). Js model still overpredicted the multiaxial ratcheting behavior. Comparison of the term $\left\langle d\boldsymbol{\varepsilon}_p : \dfrac{\boldsymbol{\alpha}_i}{\overline{\boldsymbol{\alpha}_i}}\right\rangle$ with $dp$ reduced to the multiaxial ratcheting simulation. In addition, the multiaxial parameter $B_i$ in the MD model was introduced into JS model (called as MJS model hereafter).

$$\boldsymbol{\alpha}=\sum_{i=1}^{M}\boldsymbol{\alpha}_i, \qquad d\boldsymbol{\alpha}_i=\frac{2}{3}C_i d\boldsymbol{\varepsilon}_p-\gamma_i\left(\frac{\overline{\boldsymbol{\alpha}_i}}{r_i}\right)^{m_i}\left\langle d\boldsymbol{\varepsilon}_p : \frac{\boldsymbol{\alpha}_i}{\overline{\boldsymbol{\alpha}_i}}\right\rangle\boldsymbol{\alpha}_i \tag{12}$$

where, $m_i = A_{0i}\left\langle 2-\mathbf{n}' : \dfrac{\boldsymbol{\alpha}_i}{\overline{\boldsymbol{\alpha}_i}}\right\rangle^{B_i}$, $\mathbf{n}' = \dfrac{d\boldsymbol{\varepsilon}_p}{dp} = \dfrac{3}{2\sigma_0}(\mathbf{s}-\boldsymbol{\alpha})$.

### *3.5.5 CJK model*

In order to improve the multiaxial ratcheting simulation under a large number of cycles, Chen *et al*. (2005) proposed a superposition of Prager model and OW II model.

$$\boldsymbol{\alpha}=\sum_{i=1}^{M}\boldsymbol{\alpha}_i, \qquad d\boldsymbol{\alpha}_i=\frac{2}{3}C_i d\boldsymbol{\varepsilon}_p-\gamma_i\left\langle \mathbf{n}' : \frac{\boldsymbol{\alpha}_i}{\overline{\boldsymbol{\alpha}_i}}\right\rangle^{\chi_i}\left(\frac{\overline{\boldsymbol{\alpha}_i}}{r_i}\right)^{m_i}\left\langle d\boldsymbol{\varepsilon}_p : \frac{\boldsymbol{\alpha}_i}{\overline{\boldsymbol{\alpha}_i}}\right\rangle\boldsymbol{\alpha}_i \tag{13}$$

It was shown in Eq. (13) that the term $\left\langle \mathbf{n}' : \dfrac{\boldsymbol{\alpha}_i}{\overline{\boldsymbol{\alpha}_i}}\right\rangle$ was seen as the measure of nonproportional degree. The parameter $\chi_i$ was determined from the multiaxial ratcheting test.

### *3.6 Abdel Karim-Ohno and modified Abdel Karim-Ohno models*

Abdel-Karim and Ohno (2000) proposed a superposition of the AF model and OW I model.

$$\boldsymbol{\alpha}=\sum_{i=1}^{M}\boldsymbol{\alpha}_i, \qquad d\boldsymbol{\alpha}_i=\frac{2}{3}C_i d\boldsymbol{\varepsilon}_p-\mu_i\gamma_i\boldsymbol{\alpha}_i dp-\gamma_i H(f_i)\langle d\lambda_i\rangle\boldsymbol{\alpha}_i \tag{14}$$

where $f_i=\frac{3}{2}\boldsymbol{\alpha}_i:\boldsymbol{\alpha}_i-\left(\frac{C_i}{\gamma_i\varphi(p)}\right)^2$, $d\lambda_i=d\boldsymbol{\varepsilon}_p:\frac{\boldsymbol{\alpha}_i}{C_i/\gamma_i\varphi(p)}-\mu_i dp$. The parameter $\mu_i$ was used to improve the simulation of multiaxial ratcheting behavior, but uniaxial ratcheting effect was sacrifice and shakedown phenomenon appeared. The parameter $\mu_i$ was determined by multiaxial ratcheting experimental data, the multiaxial and uniaxial ratcheting predicted results was well promoted and affected, respectively, vice versa. If $\mu_i$ = 0, the Abdel-Karim-Ohno model corresponded to the Ohno-Wang I model, which always predicted zero uniaxial ratcheting, if other sources of ratcheting were not present. On the contrary, if $\mu_i$ = 1, the Abdel-Karim-Ohno model reduced to the Chaboche model.

#### *3.6.1 Const $\mu_i$* (Abbr. AKO)

The parameters $\mu_i$ influenced ratcheting strain rate. The only one parameter $\mu = \mu_i$ was usually used for all $i$ because of simplification.

$$\mu_i=const \tag{15}$$

#### *3.6.2 Evolution of parameter $u_i$* (Abbr. AKO I)

In order to improve predictions over a relatively large number of cycles, an evolution function related to the plastic strain accumulation was introduced for $u_i$ in a manner similar to Chen and Jiao (2004). The transient effect in initial cycles, which occurred for some materials, can be described by evolution of parameter $u$ using relation.

$$d\mu_i=\omega(\mu_{i\infty}-\mu_i)dp \tag{16}$$

where $u_{i\infty}$ was the saturated value $u_i$, and $\omega$ was the evolution cofficient.

#### *3.6.3 Nonproportional term $\chi$ implemented* (Abbr. AKO II)

Further, it was difficult to simulate simulaneously the uniaxal and multiaxial ratcheting response with the AbdelKarim-Ohno model as was found by Chen and Jiao (2004). This problem was solved by introduction of nonproportional term in ratcheting parameters.

$$\mu=\eta\left\langle\frac{\partial f}{\partial\sigma}:\frac{\alpha_i}{\overline{\overline{\alpha_i}}}\right\rangle^{\chi},\quad d\eta=\omega(\eta_\infty-\eta)dp \tag{17}$$

#### *3.6.4 Evolution of parameter $\chi$* (Abbr. AKO III)

It was clear, that choice of multiaxial parameter $\chi$ influence only ratcheting under nonproportional loading (Chen *et al*. 2005). Sometimes it was useful to introduce the evolution of parameter $u$ for multiaxial parameter too.

$$\mu=\eta\left\langle\frac{\partial f}{\partial\sigma}:\frac{\alpha_i}{\overline{\overline{\alpha_i}}}\right\rangle^{\chi},\quad d\eta=\omega(\eta_\infty-\eta)dp,\quad \chi=\chi_\infty+(\chi_0-\chi_\infty)e^{-\omega_\chi p} \tag{18}$$

#### *3.6.5 Divided from $\eta$* (Abbr. AKO IV)

For a large transient effect, it was more suitable to compose increment from two parts. Furthermore, it was difficult to simulate simultaneously the uniaxial and the multiaxial ratcheting

responses with the Abdel Karim-Ohno model as was found by Chen *et al*. (2005). The problem can be solved by introduction of nonproportional term into the ratcheting parameter.

$$\mu=\eta\left\langle\frac{\partial f}{\partial\sigma}:\frac{\alpha_i}{\alpha_i}\right\rangle^{\chi},\quad d\eta=d\eta_1+d\eta_2,\quad d\eta_1=\omega_1\left(\eta_{\infty 1}-\eta_1\right)dp,\quad d\eta_2=\omega_2\left(\eta_{\infty 2}-\eta_2\right)dp \tag{19}$$

where material constant $\chi$ should be determined from a multiaxial ratcheting test. For uniaxial loading, terms $\left\langle\frac{\partial f}{\partial\sigma}:\frac{\alpha_i}{\alpha_i}\right\rangle$ became a unity and the multiaxial parameter $\chi$ was ineffective. For multiaxial loading, terms $\left\langle\frac{\partial f}{\partial\sigma}:\frac{\alpha_i}{\alpha_i}\right\rangle$ were less than a unity and the multiaxial parameter $\chi$ would influence the ratcheting response. A proper value of $\chi$ should also be found from experimental data.

### *3.6.6 Consider DSA*

Dynamic strain aging was found for stainless steel SS304 under high temperature and cyclic loading. In order to describe material deformation, the relationship between the evolution of back stress and temperature was implemented into Abdel-Karim model. The proposed model was expressed in the following. (Abbr. MKAKO)

$$\boldsymbol{\alpha}=\sum_{i=1}^{M}\boldsymbol{\alpha}_i,\quad d\boldsymbol{\alpha}_i=\frac{2}{3}C_i d\boldsymbol{\varepsilon}_p-\mu_i\gamma_i\varphi(p)\boldsymbol{\alpha}_i dp-\gamma_i\varphi(p)H(f_i)\langle d\lambda_i\rangle\boldsymbol{\alpha}_i \tag{20}$$

where $f_i=\frac{3}{2}\boldsymbol{\alpha}_i:\boldsymbol{\alpha}_i-\left(\frac{C_i}{\gamma_i\varphi(p)}\right)^2$, $d\lambda_i=d\boldsymbol{\varepsilon}_p:\frac{\boldsymbol{\alpha}_i}{C_i/\gamma_i\varphi(p)}-\mu_i dp$, the function $\varphi(p)$ represents dynamic strain aging feature, namely $\varphi\left(\varepsilon_{ep},T\right)=\varphi_\infty(T)+\left(1-\varphi_\infty(T)\right)e^{-\omega_\varphi p}$.

The disadvantage of the proposed model had not a uniform parameter that depent on the temperature. The material parameters were different under different temperatures. In order to improve the disadvantage of the proposed model, Kang *et al*. (2004) proposed that the relationship of the parameter and all the back stress, as shown in Eq. (21).

$$\mu=\frac{\mu_0}{1+a\Phi} \tag{21}$$

where the parameter $\mu_0$ and $a$ depended on the temperature, the parameter $\phi$ represented the nonproportion under multiaxial conditions. According to the work of Marquis (1987), the nonproportion was expressed in the following

$$\Phi=1-\sqrt{\frac{\dot{s}:\dot{s}}{\|s:s\|\left\|d\dot{s}:d\dot{s}\right\|}} \tag{22}$$

where $s$ and $\dot{s}$ was respectively deviation stress tensor and deviation stress tensor.

Moreover, Abdel-Karim model was modified by Halama (2008), in order to improve the predicted results. Cyclic hardening/softening and addition hardening resulted in non-proportion

loading were implemented into Abdel-Karim model, the proposed model was listed in the following. (Abbr. MHAKO)

$$\boldsymbol{\alpha}=\sum_{i=1}^{M}\boldsymbol{\alpha}_i \quad , \quad d\boldsymbol{\alpha}_i=\frac{2}{3}C_i d\boldsymbol{\varepsilon}_p-\mu_i\gamma_i\varphi(p)\boldsymbol{\alpha}_i dp-\gamma_i\varphi(p)H(f_i)\langle d\lambda_i\rangle\boldsymbol{\alpha}_i \tag{23}$$

where $f_i=\frac{3}{2}\boldsymbol{\alpha}_i:\boldsymbol{\alpha}_i-\left(\frac{C_i}{\gamma_i\varphi(p)}\right)^2$ , $d\lambda_i=d\boldsymbol{\varepsilon}_p:\frac{\boldsymbol{\alpha}_i}{C_i/\gamma_i\varphi(p)}-\mu_i dp$ , the function $\varphi(p)$ represented cyclic hardening/softening feature which was proposed by Marquis (1979), namely $\varphi(p) = \varphi_\infty + (1 - \varphi_\infty)e^{-\omega\varphi p}$. $\varphi(p) < 1$ represented cyclic hardening, $\varphi(p) < 1$ represented cyclic softening. The parameter $\mu_i$, which was lised in Eq. (24), set a ratcheting rate.

$$\mu=\eta\left\langle\frac{\partial f}{\partial\sigma}:\frac{\alpha_i}{\overline{\alpha}_i}\right\rangle^{\chi} \tag{24}$$

Further, the evolution of the parameter $\eta$ and $\chi$ were presented, in order to better describe transient ratcheting effect.

$$d\eta=d\eta_1+d\eta_2 , \quad d\eta_1=\omega_1(\eta_{\infty 1}-\eta_1)dp , \quad d\eta_2=\omega_2(\eta_{\infty 2}-\eta_2)dp \tag{25}$$

$$\chi=\chi_\infty+(\chi_0-\chi_\infty)e^{-\omega_x p} \tag{26}$$

Isotropic hardening feature was implemented into Benelallem and Calloch-Marquis (Benallal and Marqui 1987).

$$dR=b(Q-\mathrm{R})dp , \quad dq=\overline{D}(A)(Q_{AS}(A)-\mathrm{Q})dp \tag{27}$$

$$\overline{D}(A)=(d-f)\mathrm{A}+f \tag{28}$$

where $Q_{AS}(A)=\frac{gAQ_\infty+(1-A)Q_0}{gA+(1-A)}+Q_i\left|(A-1)A^n+|A-1|^n A\right|$ , $A=1-\frac{(\boldsymbol{\alpha}:d\boldsymbol{\alpha})^2}{(\boldsymbol{\alpha}:\boldsymbol{\alpha})(d\boldsymbol{\alpha}:d\boldsymbol{\alpha})}$ .

### *3.7 OW II-AF model*

Abdel-Karim model can better predict ratcheting behavior of materials for a certain cycles, which was attributed to dynamic recover $H(f_i)$ in OW I model, where $H(f_i)$ was leap function. Therefore, it was not ideal for the predicted ratcheting behavior of materials. Thus, leap function $H(f_i)$ was replaced by nonlinear term $\left(\frac{\overline{\alpha}_i}{r_i}\right)^{m_i}$ by Zhang (2002), which can better predict the ratcheting behavior of materials. AF model and OW II model were added in the following.

$$\boldsymbol{\alpha}=\sum_{i=1}^{M}\boldsymbol{\alpha}_i \quad , \quad d\boldsymbol{\alpha}_i=\frac{2}{3}C_i d\boldsymbol{\varepsilon}_p-\mu_i\gamma_i\boldsymbol{\alpha}_i dp-\gamma_i\left(\frac{\overline{\boldsymbol{\alpha}}_i}{r_i}\right)^{m_i}\langle d\lambda_i\rangle\boldsymbol{\alpha}_i \tag{29}$$

where $f_i=\frac{3}{2}\boldsymbol{\alpha}_i:\boldsymbol{\alpha}_i-\left(\frac{C_i}{\gamma_i}\right)^2$, $d\lambda_i=d\boldsymbol{\varepsilon}_p:\frac{\boldsymbol{\alpha}_i}{C_i/\gamma_i}-\mu_i dp$ (modified parameter $\mu$). Isotropic hardening feature and nonproportion were also considered by Zhang (2002).

### *3.8 Improved OW II-AF model*

The new modified model was proposed in the paper, which was inspired by the above ideas. Because OW II model was so far one of the more description ratcheting effect. Benallal and Marquis (1987) proposed that material cyclic hardening/softening function $\varphi(p)$ and the parameter $\mu_i$ were implemented into OW II-AF model. The multiaxial parameter $\chi$ was introduced into the parameter $\mu_i$. Therefore, the new modefied OW II-AF model was expressed in the following.

$$\boldsymbol{\alpha}=\sum_{i=1}^{M}\boldsymbol{\alpha}_i, \quad d\boldsymbol{\alpha}_i=\frac{2}{3}C_i d\boldsymbol{\varepsilon}_p-\mu_i\gamma_i\varphi(p)\boldsymbol{\alpha}_i dp-\gamma_i\varphi(p)\left(\frac{\overline{\boldsymbol{\alpha}_i}}{r_i}\right)^{m_i}\langle d\lambda_i\rangle\boldsymbol{\alpha}_i \tag{30}$$

where $d\lambda_i=d\boldsymbol{\varepsilon}_p:\frac{\boldsymbol{\alpha}_i}{C_i/\gamma_i\varphi(p)}-\mu_i dp$, $\varphi(p)=\varphi_\infty+(1-\varphi_\infty)e^{-\omega_\varphi p}$, $\chi=\chi_\infty+(\chi_0-\chi_\infty)e^{-\omega_\chi p}$, $\mu=\eta\left\langle\frac{\partial f}{\partial\sigma}:\frac{\alpha_i}{\overline{\alpha_i}}\right\rangle^{\chi}$, $d\eta=d\eta_1+d\eta_2$, $d\eta_1=\omega_1(\eta_{\infty 1}-\eta_1)dp$, $d\eta_2=\omega_2(\eta_{\infty 2}-\eta_2)dp$. The parameters $C_i$ and $r_i$ were determined by uniaxial tension test, similar to OW II model. $\chi$ was multiaxial ratcheting parameter. The six material constants $\eta_{01}$, $\eta_{02}$ $\eta_{\infty 1}$, $\eta_{\infty 2}$, $\omega_1$, $\omega_2$ should be determined by fitting an uniaxial ratcheting test. Marquis (1979) proposed that the function $\varphi(p)$ described the material cyclic hardening/softening feature. Kang *et al*. (2004) presented that function $\varphi(p)$ can consider dynamic strain aging, the parameters $\varphi_\infty$ and $\omega_\infty$ were the function of temperature.

## 4. Finite element implementation

### *4.1 Finite element Implementation of advanced constitutive model*

Rate-independent constitutive models had been mainly developed to simulate the ratcheting behavior of structures in the last several decades. According to ANSYS help manual (2004), rate-independent plasticity section provided the mathematical relationship that characterized the elasto-plastic response of materials. Except for user specified behavior, part of the available material behaviors in ANSYS were explained in greater details, such as bilinear and multilinear isotropic/kinematic hardening. Therefore, for user specified behavior, CJK model was taken as an example in the following to elaborate the implicit stress integration and radial return method as follows:

(1) von Mises yield criterion

$$f=\frac{3}{2}(\mathbf{s}-\boldsymbol{\alpha})^T[M_1](\mathbf{s}-\boldsymbol{\alpha})-\sigma_y=0 \tag{31}$$

where, $[M_1]$ was a non-zero auxiliary diagonal matrix, namely $[M_1]=diag[1, 1, 1, 2, 2, 2]$.

(2) Flow rule

$$d\boldsymbol{\varepsilon}^p=\frac{3}{2}\frac{\langle d\mathbf{s}\cdot\mathbf{n}\rangle}{h}\mathbf{n} \tag{32}$$

$$d\boldsymbol{\varepsilon}^p = \sqrt{\frac{3}{2}} dp[M_1] \frac{\partial f}{\partial \boldsymbol{\sigma}} \tag{33}$$

where, $dp = \sqrt{\frac{2}{3} d\boldsymbol{\varepsilon}^{pT} [M_2] d\boldsymbol{\varepsilon}^p}$, $[M_2]$ was a non-zero auxiliary diagonal matrix, namely $[M_2]$ = $diag[1, 1, 1, 1/2, 1/2, 1/2]$; $\frac{\partial f}{\partial \boldsymbol{\sigma}} = \sqrt{\frac{3}{2}} \frac{\mathbf{s}-\boldsymbol{\alpha}}{\sigma_y} = \mathbf{n}$, $h$ was plastic modulus.

(3) Strain decomposition

$$\boldsymbol{\varepsilon} = \boldsymbol{\varepsilon}^e + \boldsymbol{\varepsilon}^p \tag{34}$$

(4) Elastic strain is assumed to obey Hooke's law

$$\boldsymbol{\sigma} = D^e \boldsymbol{\varepsilon}^e = D^e \left( \boldsymbol{\varepsilon} - \boldsymbol{\varepsilon}^p \right) \tag{35}$$

5 CJK model

$$\boldsymbol{\alpha} = \sum_{i=1}^{M} \boldsymbol{\alpha}_i \tag{36}$$

$$d\boldsymbol{\alpha}_i = \frac{2}{3} C_i [M_2] d\boldsymbol{\varepsilon}^p - \gamma_i \left\langle \mathbf{n}' : \frac{\boldsymbol{\alpha}_i}{\boldsymbol{\alpha}_i} \right\rangle \left( \frac{\overline{\boldsymbol{\alpha}_i}}{r_i} \right)^{m_i} \boldsymbol{\alpha}_i \left\langle d\boldsymbol{\varepsilon}_p : \frac{\boldsymbol{\alpha}_i}{\boldsymbol{\alpha}_i} \right\rangle \tag{37}$$

where, $\mathbf{n}' = \frac{d\boldsymbol{\varepsilon}^p}{dp} = \frac{3}{2\sigma_y} (\mathbf{s}\text{-}\boldsymbol{\alpha})$.

### *4.2 Application of radial return method*

Given all constitutive variables at $t = t_n$, convergent solutions contain $\sigma_n$, $\alpha_n$, $\varepsilon_n^p$. The elastic predictor was taken to be an elastic tentative stress $\sigma_{n+1}^T$

$$\boldsymbol{\sigma}_{n+1}^T = D : \boldsymbol{\varepsilon}_{n+1}^T \tag{38}$$

$\varepsilon_{n+1}^T$ was the tentative strain

$$\boldsymbol{\varepsilon}_{n+1}^T = \boldsymbol{\varepsilon}_{n+1} - \boldsymbol{\varepsilon}_n^p \tag{39}$$

Because of elastic isotropy and plastic incompressibility, taking the deviatoric part of tentative stress $\sigma_{n+1}^T$

$$\mathbf{S}_{n+1}^T = \boldsymbol{\sigma}_{n+1}^T - \frac{1}{3} tr\left(\boldsymbol{\sigma}_{n+1}^T\right) \mathbf{I} \tag{40}$$

According to radial return method, deviatoric stress on the yield surface corresponded to tentative deviatoric stress.

$$\mathbf{S}_{n+1} = \mathbf{S}_{n+1}^T - 2G[M_2] \Delta \boldsymbol{\varepsilon}_{n+1}^p \tag{41}$$

Plastic strain increment $\Delta\varepsilon_{n+1}^{p}$

$$\Delta\boldsymbol{\varepsilon}_{n+1}^{p}=\sqrt{\frac{3}{2}}\Delta p[M_1]\mathbf{n}_{n+1} \tag{42}$$

where, $\Delta p$ was the plastic multiplier, $\mathbf{n}_{n+1}$ was the normal direction of yield surface.

$$\mathbf{n}_{n+1}=\frac{\mathbf{S}_{n+1}-\boldsymbol{\alpha}_{n+1}}{\left\|\mathbf{S}_{n+1}-\boldsymbol{\alpha}_{n+1}\right\|}=\sqrt{\frac{3}{2}}\frac{\mathbf{S}_{n+1}-\boldsymbol{\alpha}_{n+1}}{\sigma_o} \tag{43}$$

where, $n_{n+1}^{T}[M_1]\mathbf{n}_{n+1}=1,\ \ \mathbf{n}_{n+1}:\mathbf{n}_{n+1}=1$ if $f_{n+1}=0$.

Substitution of Eq. (43) into Eq. (42) provided

$$\Delta\boldsymbol{\varepsilon}_{n+1}^{p}=\frac{3}{2}\frac{\mathbf{S}_{n+1}-\boldsymbol{\alpha}_{n+1}}{\sigma_y}\Delta p \tag{44}$$

The calculation of plastic multiplier was detailedly listed in the following from CJK model

$$\boldsymbol{\alpha}_{n+1}=\boldsymbol{\alpha}_{n}+\sum_{i=1}^{M}\Delta\boldsymbol{\alpha}_{n+1}^{(i)} \tag{45}$$

$$\Delta\boldsymbol{\alpha}_{n+1}^{(i)}=\frac{2}{3}r_i\gamma_i[M_2]\Delta\boldsymbol{\varepsilon}_{n+1}^{p}-\gamma_i\sqrt{\frac{3}{2}}\left\langle\mathbf{n}_{n+1}^{T}:\frac{\boldsymbol{\alpha}_{n+1}^{(i)}}{\boldsymbol{\alpha}_{n+1}^{(i)}}\right\rangle^{\chi_i}\left(\frac{\overline{\boldsymbol{\alpha}_{n+1}^{(i)}}}{r_i}\right)^{m_i}\boldsymbol{\alpha}_{n+1}^{(i)}\left\langle\mathbf{n}_{n+1}^{T}:\frac{\boldsymbol{\alpha}_{n+1}^{(i)}}{\boldsymbol{\alpha}_{n+1}^{(i)}}\right\rangle\Delta p \tag{46}$$

$$\boldsymbol{\alpha}_{n+1}^{(i)}=\boldsymbol{\alpha}_{n}^{(i)}+\frac{2}{3}r_i\gamma_i[M_2]\Delta\boldsymbol{\varepsilon}_{n+1}^{p}-\gamma_i\sqrt{\frac{3}{2}}\left\langle\mathbf{n}_{n+1}^{T}:\frac{\boldsymbol{\alpha}_{n+1}^{(i)}}{\boldsymbol{\alpha}_{n+1}^{(i)}}\right\rangle^{\chi_i}\left(\frac{\overline{\boldsymbol{\alpha}_{n+1}^{(i)}}}{r_i}\right)^{m_i}\boldsymbol{\alpha}_{n+1}^{(i)}\left\langle\mathbf{n}_{n+1}^{T}:\frac{\boldsymbol{\alpha}_{n+1}^{(i)}}{\boldsymbol{\alpha}_{n+1}^{(i)}}\right\rangle\Delta p \tag{47}$$

$$\boldsymbol{\alpha}_{n+1}^{(i)}=\theta_{n+1}^{(i)}\left(\boldsymbol{\alpha}_{n}^{(i)}+\frac{2}{3}r_i\gamma_i[M_2]\Delta\boldsymbol{\varepsilon}_{n+1}^{p}\right) \tag{48}$$

$$\theta_{n+1}^{(i)}=\frac{1}{1+\gamma_i\sqrt{\frac{3}{2}}\left\langle\mathbf{n}_{n+1}^{T}:\frac{\boldsymbol{\alpha}_{n+1}^{(i)}}{\boldsymbol{\alpha}_{n+1}^{(i)}}\right\rangle^{\chi_i}\left(\frac{\overline{\boldsymbol{\alpha}_{n+1}^{(i)}}}{r_i}\right)^{m_i}\left\langle\mathbf{n}_{n+1}^{T}:\frac{\boldsymbol{\alpha}_{n+1}^{(i)}}{\boldsymbol{\alpha}_{n+1}^{(i)}}\right\rangle\Delta p} \tag{49}$$

Eq. (48) subtracted from Eq. (41) gave

$$\mathbf{S}_{n+1}-\boldsymbol{\alpha}_{n+1}=\mathbf{S}_{n+1}^{T}-2G[M_2]\Delta\boldsymbol{\varepsilon}_{n+1}^{p}-\sum_{i=1}^{M}\theta_{n+1}^{(i)}\left(\boldsymbol{\alpha}_{n}^{(i)}+\frac{2}{3}r_i\gamma_i[M_2]\Delta\boldsymbol{\varepsilon}_{n+1}^{p}\right) \tag{50}$$

Eq. (48) subtracted from Eq. (41) gave

$$\mathbf{S}_{n+1}-\boldsymbol{\alpha}_{n+1}=\left(\mathbf{S}_{n+1}^{T}-\sum_{i=1}^{M}\theta_{n+1}^{(i)}\boldsymbol{\alpha}_{n}^{(i)}\right)/\left(1+3G\Delta p/\sigma_y-\sum_{i=1}^{M}r_i\gamma_i\theta_{n+1}^{(i)}\Delta p/\sigma_y\right) \tag{51}$$

$\mathbf{S}_{n+1} - \boldsymbol{\alpha}_{n+1}$ should satisfy yield function, namely Eq. (31), thus plastic multiplier was expressed as follows.

$$\Delta p = \frac{\left[\frac{3}{2}\left(\mathbf{S}_{n+1}^{T} - \sum_{i=1}^{M}\theta_{n+1}^{(i)}\boldsymbol{\alpha}_{n}^{(i)}\right)^{T}[M_1]\left(\mathbf{S}_{n+1}^{T} - \sum_{i=1}^{M}\theta_{n+1}^{(i)}\boldsymbol{\alpha}_{n}^{(i)}\right)\right]^{\frac{1}{2}} - \sigma_y}{3G + \sum_{i=1}^{M} r_i\gamma_i\theta_{n+1}^{(i)}} \tag{52}$$

Iterative calculation was applied in the calculation of plastic multiplier. Iterative calculation was convergent if satisfying in the following condition.

$$\left|\Delta p(k+1) - \Delta p(k)\right| \le eps \tag{53}$$

Iterative convergence represented tentative success. Then, plastic strain increment, stress and plastic strain would be provided.

$$\Delta\boldsymbol{\varepsilon}^{p} = \Delta p(k+1)\sqrt{\frac{3}{2}}[M_1]\mathbf{n}_{n+1} \tag{54}$$

$$\boldsymbol{\sigma}_{n+1} = D : \left(\boldsymbol{\varepsilon}_{n+1}^{tr} - \Delta\boldsymbol{\varepsilon}^{p}\right) \tag{55}$$

$$\boldsymbol{\varepsilon}_{n+1}^{p} = \boldsymbol{\varepsilon}_{n}^{p} + \Delta\boldsymbol{\varepsilon}_{n+1}^{p} \tag{56}$$

The above process was shown in Fig. 20.

Consistent tangent modulus was derived as follows.

$$\frac{d\Delta\sigma_{n+1}}{d\Delta\boldsymbol{\varepsilon}_{n+1}} = D^{e} - 4G^{2}L_{n+1}^{-1} : I_d \tag{57}$$

$$L_{n+1} = 2G\mathbf{I} + \sum_{i=1}^{M}\mathbf{H}_{n+1}^{(i)} + \frac{2}{3}\left(\frac{dY}{dp}\right)_{n+1}\mathbf{n}_{n+1}\otimes\mathbf{n}_{n+1} + \frac{2}{3}\frac{Y_{n+1}}{\Delta p_{n+1}}\left(\mathbf{I} - \mathbf{n}_{n+1}\otimes\mathbf{n}_{n+1}\right) \tag{58}$$

$\mathbf{H}_{n+1}^{(i)}$ in Eq. (58) was fourth-rank constitutive parameters. In order to obtain $\mathbf{H}_{n+1}^{(i)}$, differentiating Eq. (48) to have

$$d\Delta\boldsymbol{\alpha}_{n+1}^{(i)} = \frac{2}{3}r_i\gamma_i\theta_{n+1}^{(i)}[M_2]d\Delta\boldsymbol{\varepsilon}_{n+1}^{p} + \frac{d\theta_{n+1}^{(i)}}{\theta_{n+1}^{(i)}}\boldsymbol{\alpha}_{n+1}^{(i)} \tag{59}$$

Differentiation Eq. (49) and use of Eq. (42) allowed $d\theta_{n+1}^{(i)}$ to be expressed as follows.

$$d\theta_{n+1}^{(i)} = -\sqrt{\frac{2}{3}}\theta_{n+1}^{(i)\,2}\gamma_i\left\langle\mathbf{n}_{n+1}^{T} : \frac{\boldsymbol{\alpha}_{n+1}^{(i)}}{\overline{\boldsymbol{\alpha}_{n+1}^{(i)}}}\right\rangle^{\chi_i}\left(\frac{\overline{\boldsymbol{\alpha}_{n+1}^{(i)}}}{r_i}\right)^{m_i}\left\langle\mathbf{n}_{n+1}^{T} : \frac{\alpha_{n+1}^{(i)}}{\overline{\alpha_{n+1}^{(i)}}}\right\rangle\mathbf{n}_{n+1}^{T} : d\Delta\boldsymbol{\varepsilon}_{n+1}^{p} \tag{60}$$

Substitution of Eq. (60) into Eq. (59) provided

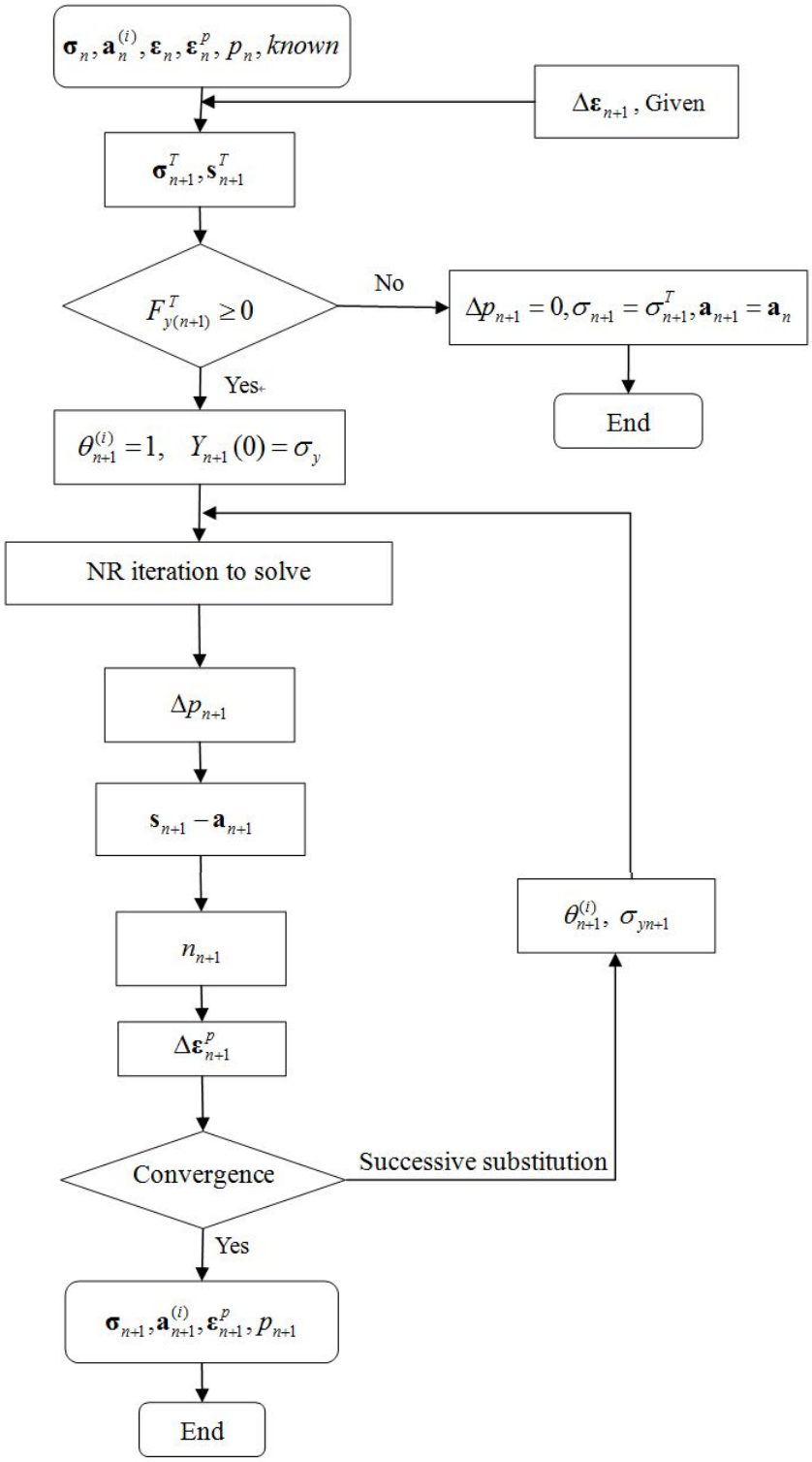


Fig. 20 Flow diagram of radial return algorithm

$$d\Delta\boldsymbol{\alpha}_{n+1}^{(i)}=\frac{2}{3}r_i\gamma_i\theta_{n+1}^{(i)}\left([M_2]-\sqrt{\frac{3}{2}}\left\langle\mathbf{n}_{n+1}^T:\frac{\boldsymbol{\alpha}_{n+1}^{(i)}}{\boldsymbol{\alpha}_{n+1}^{(i)}}\right\rangle^{\chi_i}\left(\frac{\overline{\boldsymbol{\alpha}_{n+1}^{(i)}}}{r_i}\right)^{m_i}\frac{\boldsymbol{\alpha}_{n+1}^{(i)}}{r_i}\left\langle\mathbf{n}_{n+1}^T:\frac{\boldsymbol{\alpha}_{n+1}^{(i)}}{\boldsymbol{\alpha}_{n+1}^{(i)}}\right\rangle\mathbf{n}_{n+1}^T\right):d\Delta\boldsymbol{\varepsilon}_{n+1}^p \tag{61}$$

Here, $\mathbf{m}_{n+1}^{(i)}=\sqrt{\frac{3}{2}}\frac{\boldsymbol{\alpha}_{n+1}^{(i)}}{r_i}$ or $\mathbf{m}_{n+1}^{(i)}=\sqrt{\frac{3}{2}}\frac{\boldsymbol{\alpha}_{n+1}^{(i)}}{\boldsymbol{\alpha}_{n+1}^{(i)}}$, $\overline{\boldsymbol{\alpha}_{n+1}^{(i)}}=\sqrt{\frac{3}{2}\left\{\boldsymbol{\alpha}_{n+1}^{(i)}\right\}^T[M_1]\left\{\boldsymbol{\alpha}_{n+1}^{(i)}\right\}}$.

For the CJK model, therefore, fourth-rank constitutive parameters $\mathbf{H}_{n+1}^{(i)}$ of consistent tangent modulus had an expression.

$$\mathbf{H}_{n+1}^{(i)}=\frac{d\Delta\boldsymbol{\alpha}_{n+1}^{(i)}}{d\Delta\boldsymbol{\varepsilon}_{n+1}^p}=\frac{2}{3}r_i\gamma_i\theta_{n+1}^i\left([M_2]-\mathbf{m}_{n+1}^{(i)}\mathbf{n}_{n+1}^T\left\langle\mathbf{n}_{n+1}^T:\frac{\boldsymbol{\alpha}_{n+1}^{(i)}}{\boldsymbol{\alpha}_{n+1}^{(i)}}\right\rangle^{\chi_i}\left(\frac{\overline{\boldsymbol{\alpha}_{n+1}^{(i)}}}{r_i}\right)^{m_i}\left\langle\mathbf{n}_{n+1}^T:\frac{\boldsymbol{\alpha}_{n+1}^{(i)}}{\boldsymbol{\alpha}_{n+1}^{(i)}}\right\rangle\right) \tag{62}$$

In order to obtain plastic modulus, substitution of Eq. (32) into Eq. (46) provided

$$d\boldsymbol{\alpha}_{n+1}^{(i)}=r_i\gamma_i\frac{d\mathbf{s}_{n+1}\cdot\mathbf{n}_{n+1}}{h}\mathbf{n}_{n+1}-\gamma_i\sqrt{\frac{3}{2}}\left\langle\mathbf{n}':\frac{\boldsymbol{\alpha}_{n+1}^{(i)}}{\boldsymbol{\alpha}_{n+1}^{(i)}}\right\rangle^{\chi_i}\left(\frac{\overline{\boldsymbol{\alpha}_{n+1}^{(i)}}}{r_i}\right)^{m_i}\boldsymbol{\alpha}_{n+1}^{(i)}\left\langle\mathbf{n}_{n+1}^T:\frac{\boldsymbol{\alpha}_{n+1}^{(i)}}{\boldsymbol{\alpha}_{n+1}^{(i)}}\right\rangle\mathbf{n}_{n+1}^T dp \tag{63}$$

Then, substitution of Eq. (33) into Eq. (63), and both sides multiplied by $\mathbf{n}_{n+1}$, provided

$$h=\sum_{i=1}^{M}r_i\gamma_i-\sqrt{\frac{3}{2}}\mathbf{n}^T[M_1]\sum_{i=1}^{M}\gamma_i\boldsymbol{\alpha}_i\left(\frac{\overline{\boldsymbol{\alpha}_i}}{r_i}\right)^{m_i}\left\langle\mathbf{n}^T:\frac{\boldsymbol{\alpha}^{(i)}}{\boldsymbol{\alpha}_i}\right\rangle^{\chi_i}\left\langle\mathbf{n}^T:\frac{\boldsymbol{\alpha}^{(i)}}{\boldsymbol{\alpha}_i}\right\rangle \tag{64}$$

For the CJK model, therefore, plastic modulus $h$ had an expression

$$h=\sum_{i=1}^{M}r_i\gamma_i-\sqrt{\frac{3}{2}}\mathbf{n}^T[M_1]\sum_{i=1}^{M}\gamma_i\boldsymbol{\alpha}_i\left(\frac{\overline{\boldsymbol{\alpha}_i}}{r_i}\right)^{m_i}\left\langle\mathbf{n}^T:\frac{\boldsymbol{\alpha}^{(i)}}{\boldsymbol{\alpha}_i}\right\rangle^{\chi_i}\left\langle\mathbf{n}^T:\frac{\boldsymbol{\alpha}^{(i)}}{\boldsymbol{\alpha}_i}\right\rangle \tag{65}$$

## 5. Application of FEA

The determination parameters of the above constitutive models were shown in the following.

### *5.1 Material experiments for model parameter determination*

#### *5.1.1 BKH model*

BKH model was a simple bi-linear kinematic model. The strain-stress curve of uniaxial tension was shown in Fig. 21(a). It was found that the elastic modulus was $E = 1.95 \times 10^5$ MPa, Tangential modulus was $E_T = 2850$ MPa. Figs. 21(b)~(c) showed respectively material strain-cycling and uniaxial ratcheting behavior. It was seen from Figs. 21(b)~(c) that BKH model overpredicted yield stress of hysteresis curve, underpredicted uniaxial ratcheting strain and reached shakedown state.

### *5.1.2 MKIN/KINH model*

#### *5.1.2.1 MKIN model*

MKIN model, which was composed of several linear segments, was a multilinear kinematic model. MKIN model allowed to define up to five stress-strain curves for temperature dependent properties. Each curve contained five data points. Comparison of Figs. 21 and 22 indicated that the predicted results of MKIN model were in well agreement with those of BKH model. The predicted results of MKIN model were similar with those of BKH model for uniaxial ratcheting behavior. Uniaxial ratcheting strain was both underpredicted and shakedown state appeared.

#### *5.1.2.2 KINH model*

Similar with MKIN model, KINH model, which applied in Rice model, was also a multilinear kinematic model. KINH model allowed defining more stress-strain curves for temperature dependent properties. Each curve should contain the same number of points. Comparison of Figs.

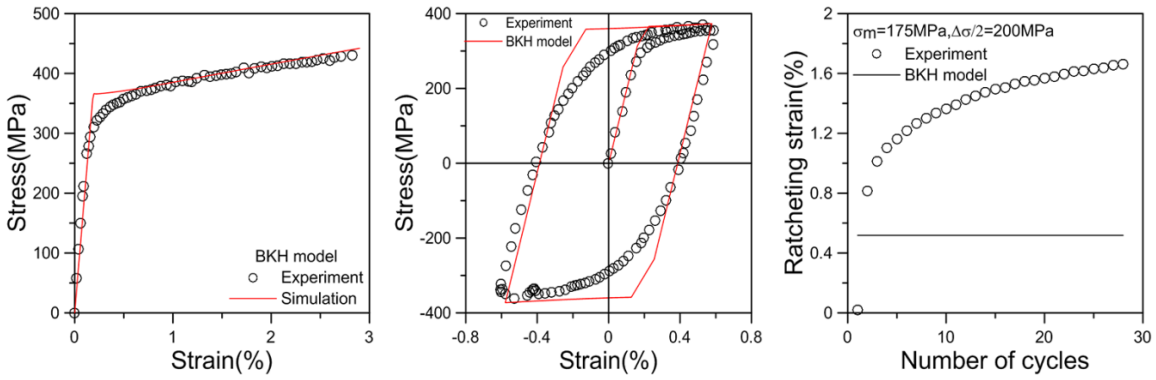


(a) (b) (c)

Fig. 21 Parameter determination for the BKH model: (a) uniaxial tension; (b) hysteresis hoop; (c) uniaxial ratcheting

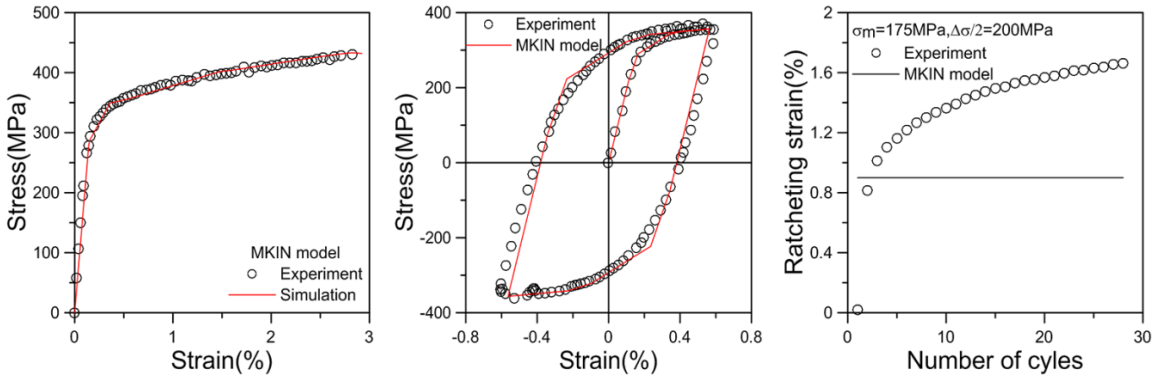


(a) (b) (c)

Fig. 22 Parameter determination for the MKIN model: (a) uniaxial tension; (b) hysteresis hoop; (c) uniaxial ratcheting

22 and 23 indicated that the predicted results of KINH model were in well agreement with those of MKIN model. The linear kinematic model such as BKH model, MKIN model and KINH predicted the similar uniaxial ratcheting behavior and shakedown state.

### *5.1.3 Armstrong-Frederic model*

Armstrong-Frederic model, which contained two parameters determined by unaxial tension curve (Fig. 24(a)), was a famous nonlinear kinematic model. It was seen from Fig. 24(b) that AF model underpredicted the yield stress of hysteresis hoop. AF model, which was compared with linear kinematic model such as BKH model, MKIN model and KINH model, was a leap of the development history of cyclic plasticity constitutive model.

### *5.1.4 Chaboche model with isotropic hardening rule and without isotropic hardening rule*

Isotropic hardening rule was implemented into AF type constitutive model in the paper. Strain

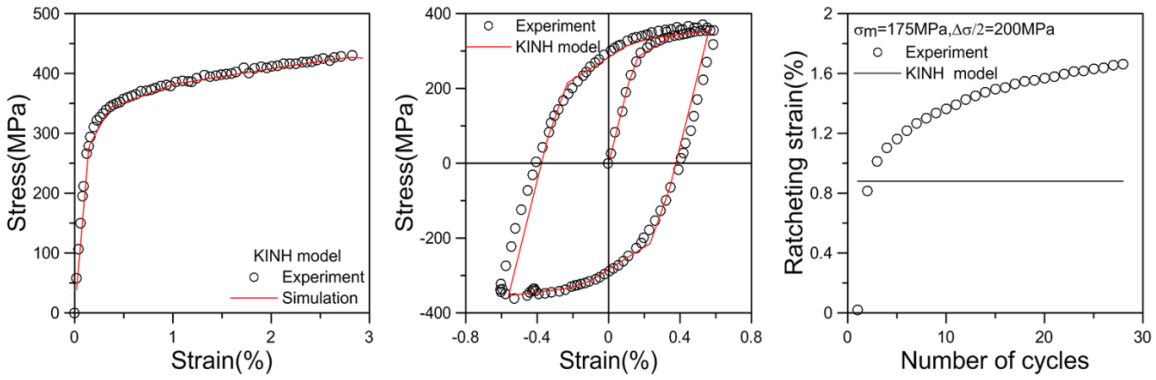


(a) (b) (c)

Fig. 23 Parameter determination for the KINH model: (a) uniaxial tension; (b) hysteresis hoop; (c) uniaxial ratcheting

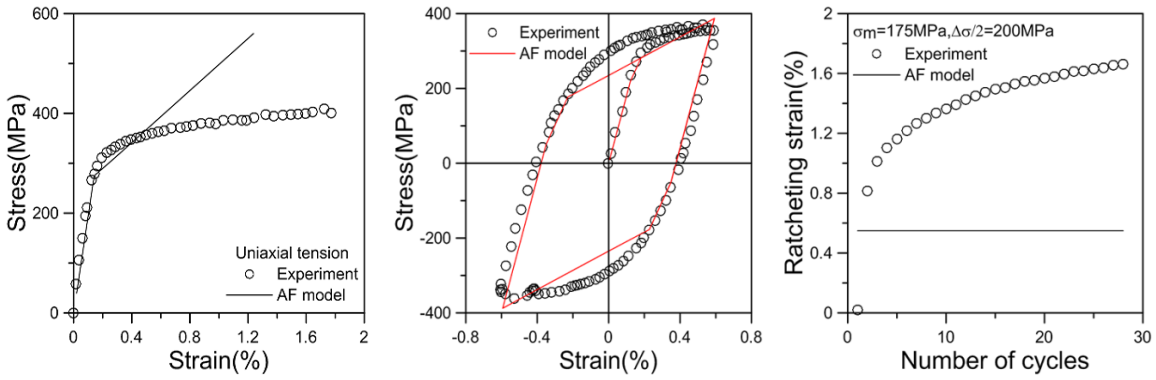


(a) (b) (c)

Fig. 24 Parameter determination for the AF model: (a) uniaxial tension; (b) hysteresis hoop; (c) uniaxial ratcheting

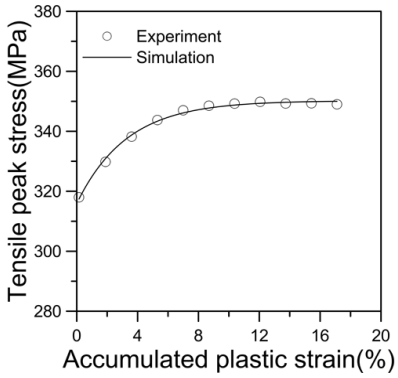


Fig. 25 Sketch map of simulating the parameters of isotropic hardening rule $Q$ and $b$

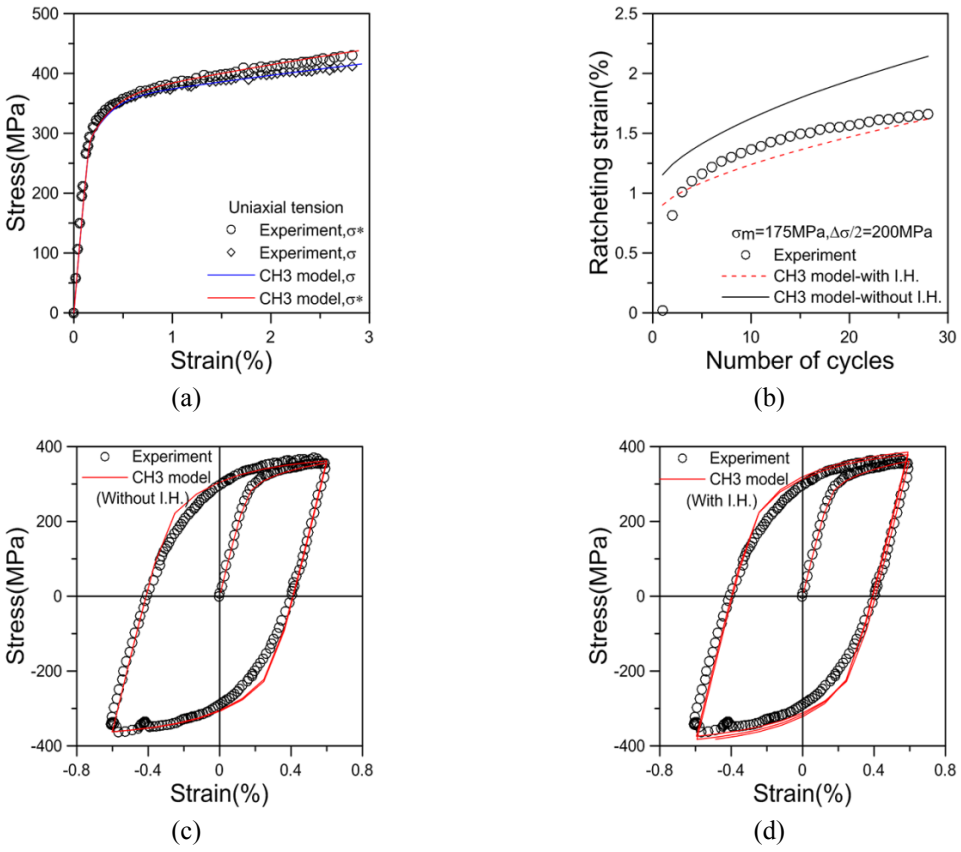


Fig. 26 Parameter determination for the Chaboche model: (a) uniaxial tension; (b) uniaxial ratcheting; (c) hysteresis hoop without I.H.; (d) hysteresis hoop with I.H.

hardening of uniaxial tension cannot be described by means of isotropic hardening rule. Thus, the parameters of isotropic hardening rule were determined by the reference (Kang *et al*. 2004). The increment of isotropic hardening rule was deducted from uniaxial tension curve, namely $\sigma^* = \sigma -$

Table 3 The parameters of CH3 model with and without isotropic hardening rule

| Temperature (°C) | $E$ (GPa) | $\sigma_y^0$ (MPa) | $C_{1\text{-}3}$ (MPa) | $\gamma_{1\text{-}3}$ | $Q$ | $b$ |
|---|---|---|---|---|---|---|
| 25 | 195 | 100 | $4.0\times10^6$, $1.5\times10^5$, 2500 | $4.0\times10^4$, 870, 4.5 | - | - |
| 25 | 195 | 100 | $4.0\times10^6$, $1.5\times10^5$, 2500 | $4.0\times10^4$, 870, 4.5 | 30 | 34 |
| 150 | 180 | 82 | $4.0\times10^6$, $1.1\times10^5$, 2500 | $4.0\times10^4$, 900, 4.5 | - | - |
| 250 | 170 | 76.7 | $4.0\times10^6$, $0.9\times10^5$, 2500 | $4.0\times10^4$, 900, 4.5 | - | - |
| 350 | 165 | 60 | $4.0\times10^6$, $0.9\times10^5$, 2500 | $4.0\times10^4$, 950, 4.5 | - | - |

$Q(1 - (\exp - b\varepsilon_p))$. The parameters $Q$ and $b$ were determined by the least squares fitting method of the curve of peak stress and accumulated plastic strain extracted from strain cycling test data, as shown in Fig. 25.

Fig. 26 gave the simulation of uniaxial tension, strain cycling and uniaxial ratcheting data with CH3 model. CH3 model, which was relatively better used to predict the ratcheting strain model, was in the finite element software ANSYS. The parameters of CH3 model were determined by

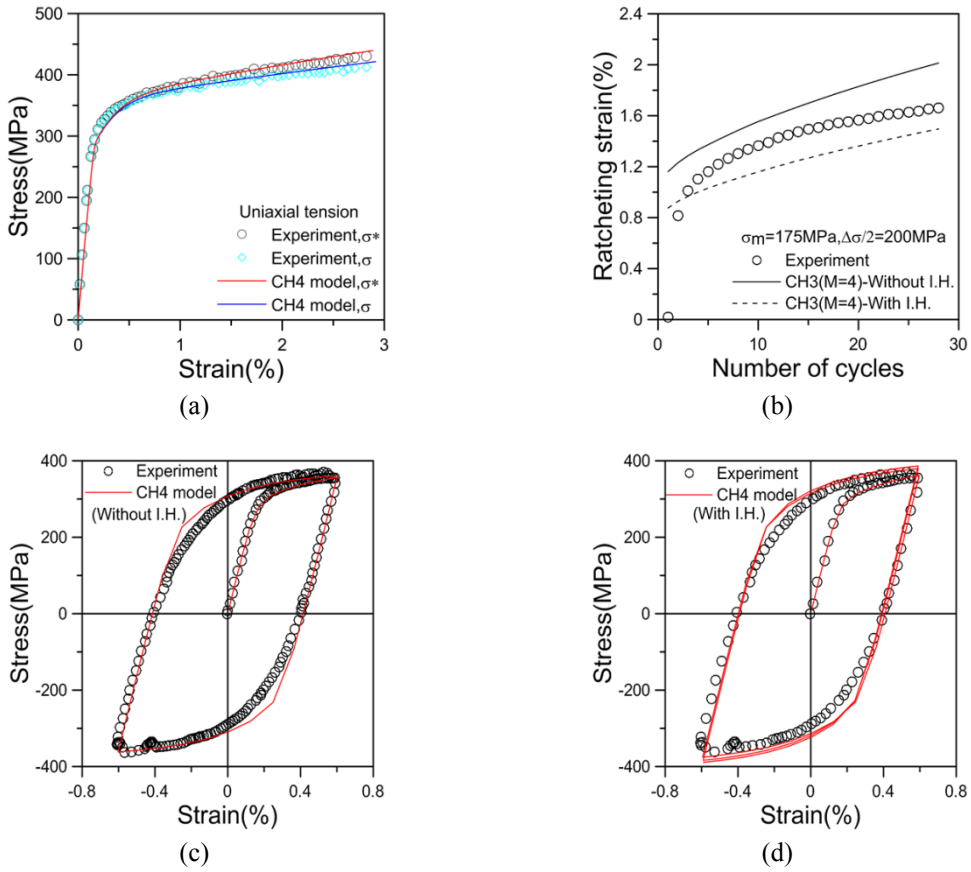


Fig. 27 Parameter determination for the Chaboche ($M = 5$) model: (a) uniaxial tension; (b) uniaxial ratcheting; (c) hysteresis hoop without I.H.; (d) hysteresis hoop with I.H.

Table 4 Parameter determination for the CH4 model with and without isotropic hardening rule

| Test type | Parameters |
|---|---|
| Uniaxial tension (no isotropic hardening) | $\sigma_y$ = 100 MPa, $C_1$ = 400000 MPa, $\gamma_1$ = 23000, $C_2$ = 38000 MPa, $\gamma_2$ = 510, $C_3$ = 2300 MPa, $\gamma_3$ = 4.5, $C_4$ = 1000000 MPa, $\gamma_4$ = 85000 |
| Uniaxial tension (isotropic hardening) | $\sigma_y$ = 100 MPa, $C_1$ = 400000 MPa, $\gamma_1$ = 23000 MPa, $C_2$ = 38000 MPa, $\gamma_2$ = 480, $C_3$ = 2300 MPa, $\gamma_3$ = 4.5, $C_4$ = 1000000 MPa, $\gamma_4$ = 85000 $\overline{\alpha}_4$ = 50, $b$ = 30, $Q$ = 34 |

uniaxial tension curve and uniaxial ratcheting test data, according to Bari and Hassan's proposed method (2000). The uniaxial tension curve, strain cycling and uniaxial ratcheting effect using CH3 model with and without isotropic hardening rule were also showed in the Fig. 26. The parameters of CH3 model with and without isotropic hardening rule were listed in the Table 3.

#### *5.1.5 Chaboche model (M = 4) with isotropic hardening rule and without isotropic hardening rule*

The uniaxial tension curve, strain cycling and uniaxial ratcheting effect using CH4 model with and without isotropic hardening rule were also showed in the Fig. 27. CH4 model was CH3 model implemented into four decomposed rule of threshold term. Therefore, the predicted uniaxial ratcheitng strain of CH4 model was smaller than that of CH3 model. The parameters of CH4 model with and without isotropic hardening rule were listed in the Table 4.

#### *5.1.6 Ohno-Wang model I with isotropic hardening rule and without isotropic hardening rule*

For uniaxial ratcheting case, OW I model produced a close hysteresis hoop, and no ratcheting strain occurred. Therefore, OW I model was not widely used, but it was a solid foundation for the development of new constitutive model. Uniaxial tension curve and strain cycling using OW I model with and without isotropic hardening rule were given in Fig. 28. Table 5 gave the parameters of OW I model with and without isotropic hardening rule.

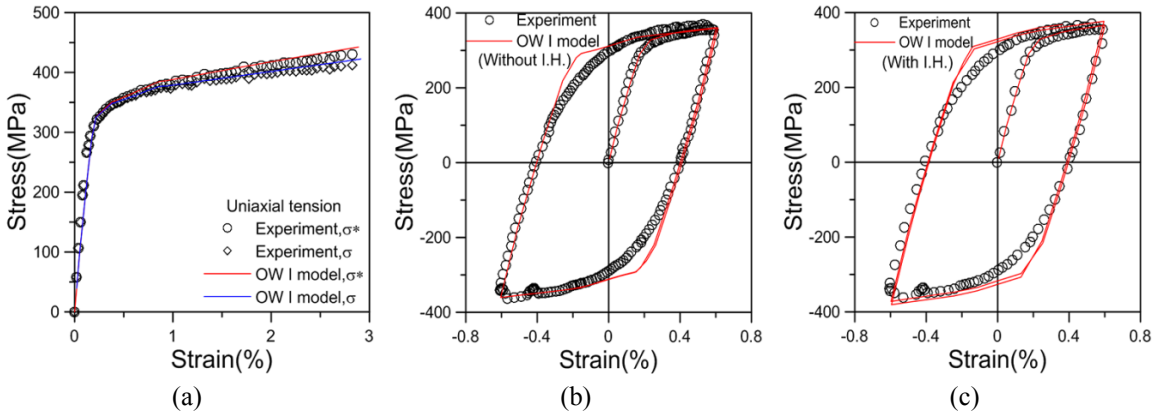


Fig. 28 Parameter determination for the OW I model: (a) uniaxial tension; (b) ysteresis hoop without I.H.; (c) hysteresis hoop with I.H.

Table 5 Parameter determination for OW I model with and without isotropic hardening rule

| Test type | Parameters |
|---|---|
| Uniaxial tension (no isotropic hardening) | $\sigma_y$ = 100 MPa, $C_1$ = 400000 MPa, $\gamma_1$ = 8000 MPa, $C_2$ = 42000, $\gamma_2$ = 4000, $C_3$ = 120000, $\gamma_3$ = 2000, $C_4$ = 8000, $\gamma_4$ = 500 $C_5$ = 4000, $\gamma_5$ = 150, $C_6$ = 2200, $\gamma_6$ = 20 |
| Uniaxial tension (isotropic hardening) | $\sigma_y$ = 100 MPa, $C_1$ = 400000 MPa, $\gamma_1$ = 8000 MPa, $C_2$ = 42000, $\gamma_2$ = 4000, $C_3$ = 120000, $\gamma_3$ = 2000, $C_4$ = 8000, $\gamma_4$ = 500 $C_5$ = 4200, $\gamma_5$ = 150, $C_6$ = 2300, $\gamma_6$ = 20, $b$ = 30, $Q$ = 34 |

### *5.1.7 Ohno-Wang model II with isotropic hardening rule and without isotropic hardening rule*

OW II model, which avoided the disadvantage of OW I model, was so far widely used to predict ratcheting behavior of materials or structures. Comparison of Figs. 28 and 29, which indicated the better predicted results of OW II model such as uniaxial tension cuvre and, ratcheting strain and strain cycling. Table 6 gave the parameters of OW I model with and without isotropic hardening rule. Moreover, Mc model, JS model, MJS model and CJK model was developed based

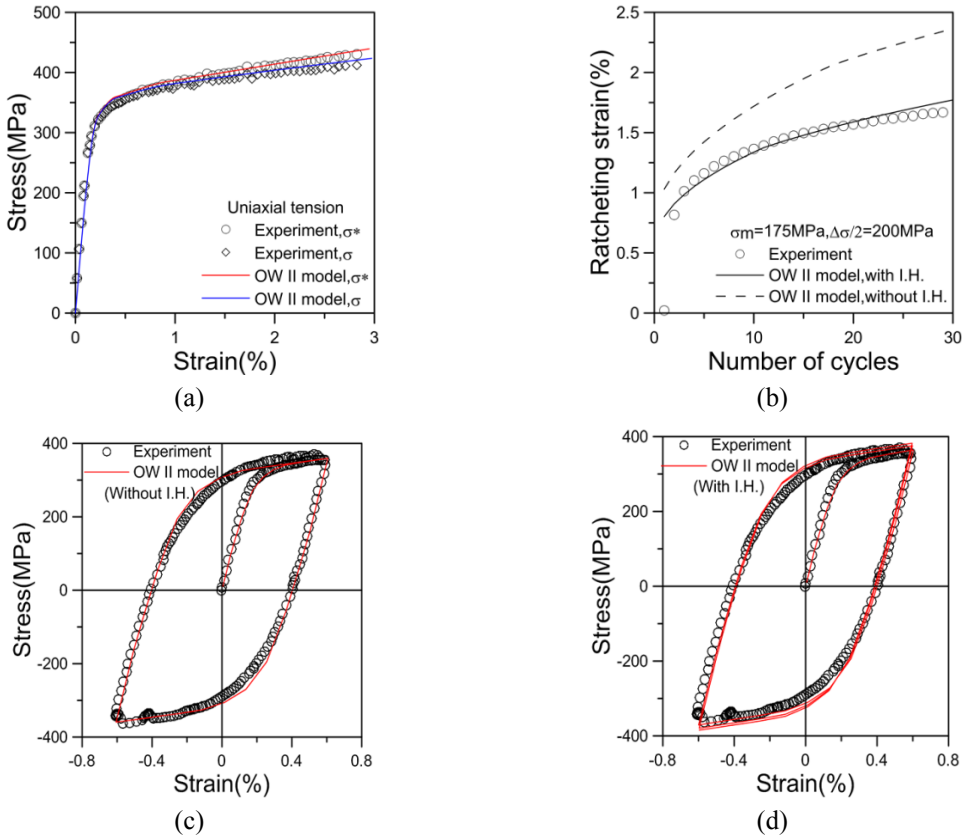


Fig. 29 Parameter determination for the OW II model: (a) uniaxial tension; (b) uniaxial ratcheting; (c) hysteresis hoop without I.H.; (d) hysteresis hoop with I.H.

Table 6 Parameter determination for OW II model with and without isotropic hardening rule

| Test type | Parameters |
|---|---|
| Uniaxial tension (no isotropic hardening) | $\sigma_y$ = 100 MPa, $C_1$ = 400000 MPa, $\gamma_1$ = 8000 MPa, $C_2$ = 42000, $\gamma_2$ = 4000, $C_3$ = 124000, $\gamma_3$ = 2000, $C_4$ = 10000, $\gamma_4$ = 500, $C_5$ = 4200, $\gamma_5$ = 150, $C_6$ = 2200, $\gamma_6$ = 20, $m_i$ = 4.5 |
| Uniaxial tension (isotropic hardening) | $\sigma_y$ = 100 MPa, $C_1$ = 400000 MPa, $\gamma_1$ = 8000 MPa, $C_2$ = 42000, $\gamma_2$ = 4000, $C_3$ = 124000, $\gamma_3$ = 2000, $C_4$ = 10000, $\gamma_4$ = 500, $C_5$ = 4500, $\gamma_5$ = 150, $C_6$ = 2200, $\gamma_6$ = 20, $m_i$ = 4.5, $b$ = 30, $Q$ = 34 |

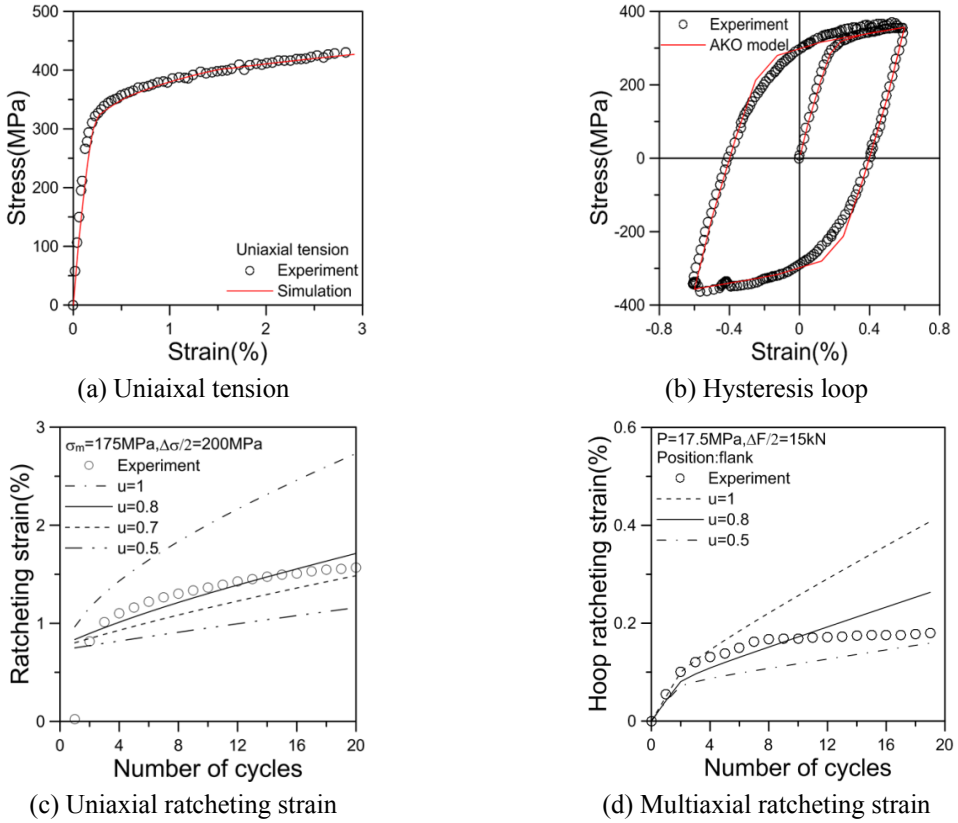


(a) Uniaxial tension (b) Hysteresis loop

(c) Uniaxial ratcheting strain (d) Multiaxial ratcheting strain

Fig. 30 Parameter determination and simulation of hysteresis loop and uniaxial ratcheting effect by AKO model

on OW II model, so the parameters of those models were the same except multiaxial ratcheting parameters.

### *5.1.8 Abdel Karim-Ohno and modified Abdel Karim-Ohno models*

#### *5.1.11.1 Const $\mu_i$*

IF the parameter $\mu_i$ was const, it was determined by uniaxial ratcheting behavior. It was seen from Fig. 30(a) that ratcheting strain rate increased with the increasing of the parameter $\mu_i$. Abdel Karim-Ohno model was close characteristics of CH3 model for the larger parameter $\mu_i$. Thus, it

ocerpredicted ratcheting strain, ratcheting strain rate was const.

#### *5.1.11.2 Divided from η*

Assuming only parameter $u_i$ for ratcheting transient effect in initial cycles and a larger transient effect could be introduced into Abdel Karim-Ohno model. The parameter $\eta$ was divided into two parts. The parameters, which were listed in Table 7, were determined by the reference (Halama 2008). The experiemental and predicted results of uniaxial tension, strain cycling and uniaxial ratcheting behavior of OW I–AF model (AKO IV) were shown in Fig. 31.

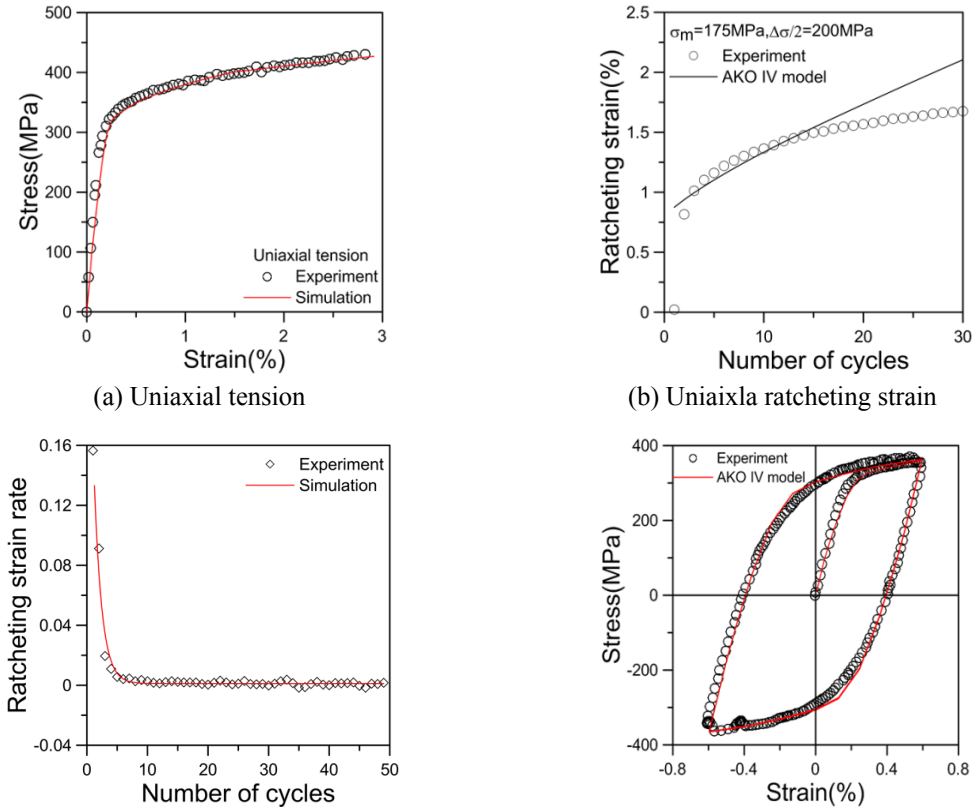


Fig. 31 Parameter determination and simulation of hysteresis loop and uniaxial ratcheting effect by AKO IV model

Table 7 The material parameters of AKO IV model

| Test type | Parameters |
|---|---|
| Uniaxial tension | $\sigma_y$ = 100 MPa, $C_1$ = 320000 MPa, $\gamma_1$ = 8000 MPa, $C_2$ = 428000 MPa, $\gamma_2$ = 4000, $C_3$ = 1240000, $\gamma_3$ = 2000, $C_4$ = 9000 MPa, $\gamma_4$ = 500, $C_5$ = 9000 MPa, $\gamma_5$ = 150, $C_6$ = 2200 MPa, $\gamma_6$ = 20 |
| Uniaxial ratcheting test | $\eta_{01}$ = 0.5, $\omega_1$ = 1.5, $\eta_{\infty 1}$ = 0.4, $\eta_{02}$ = 0.3, $\omega_2$ = 1, $\eta_{\infty 2}$ = 0.3 |
| Multiaxial ratcheting test | $\chi$ = 3 |

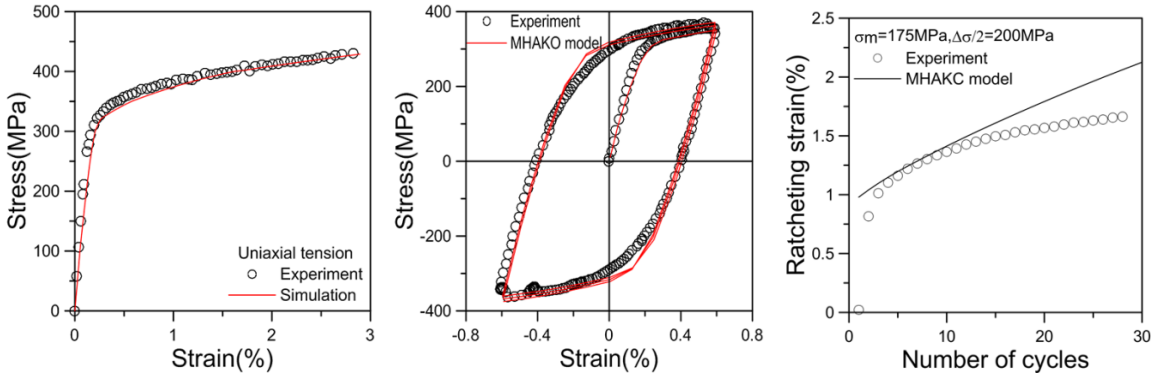


(a) Uniaxial tension (b) Hysteresis loop (c) Uniaixla ratcheting strain

Fig. 32 Parameter determination and simulation of hysteresis loop and uniaxial ratcheting effect by MHAKO model

Table 8 The material parameters of MHAKO model

| Test type | Parameters |
|---|---|
| Uniaxial tension | $\sigma_y$ = 100 MPa, $C_1$ = 400000 MPa, $\gamma_1$ = 8000 MPa, $C_2$ = 400000 MPa, $\gamma_2$ = 4000, $C_3$ = 1240000 MPa, $\gamma_3$ = 2000, $C_4$ = 10000 MPa, $\gamma_4$ = 500, $C_5$ = 4200 MPa, $\gamma_5$ = 150, $C_6$ = 2200 MPa, $\gamma_6$ = 20 |
| Uniaxial ratcheting test | $\eta_{01}$ = 0.5, $\omega_1$ = 1.5, $\eta_{\infty 1}$ = 0.4, $\eta_{02}$ = 0.3, $\omega_2$ = 1, $\eta_{\infty 2}$ = 0.3 |
| Multiaxial ratcheting test | $\chi$ = 3 |
| Tem. dependent parameter | $\varphi_\infty$ = 0.8, $\omega_\varphi$ = 15 |

### *5.1.9 OW I-AF model*

Fig. 32 gave the experiemental and predicted results of uniaxial tension, strain cycling and uniaxial ratcheting behavior of OW I–AF model (MHAKO). The parameters of OW I-AF model were shown in the Table 8. It was seem from Fig. 32 (b) that the function $\varphi(p)$ indicated cyclic hardening feature.

### *5.1.10 OW II-AF model*

The experiemental and predicted results of uniaxial tension, strain cycling and uniaxial ratcheting behavior of OW II–AF model were shown in Fig. 33. It was seem from Fig. 33 that the trends of the predicted results of OW II-AF model was in well agreement with experimental data, but slgihtly larger. This was attributed to nonlinear term $\left(\frac{\overline{\alpha}_i}{r_i}\right)^{m_i}$. The parameters of OW II-AF model were shown in the Table 9.

### *5.1.11 A new modified OW II-AF model*

The experiemental and predicted results of uniaxial tension, strain cycling and uniaxial ratcheting behavior of the modified OW II–AF model were shown in Fig. 34. It was seem from Fig. 34 that the trends of the predicted results of the modified OW II-AF model was in well

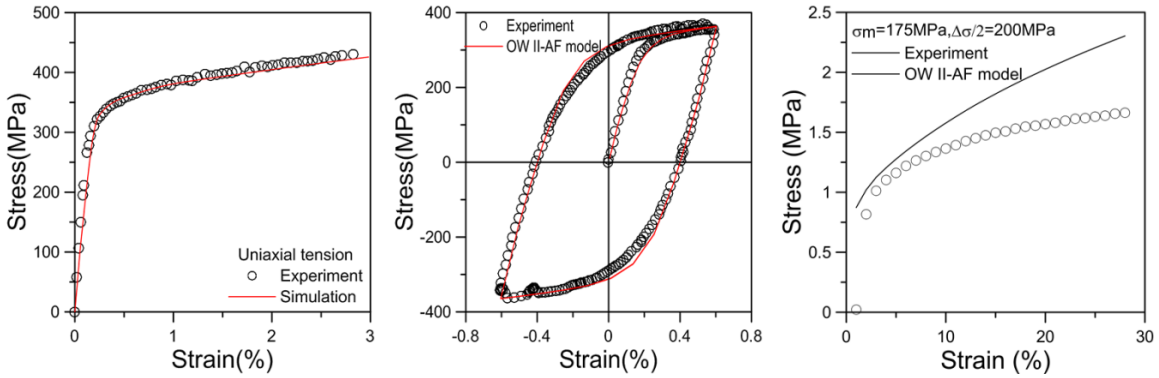


(a) Uniaxial tension (b) Hysteresis loop (c) Uniaixla ratcheting strain

Fig. 33 Parameter determination and simulation of hysteresis loop and uniaxial ratcheting by OW II-AF model

Table 9 The material parameters of OW II-AF model

| Test type | Parameters |
|---|---|
| Uniaxial tension | $\sigma_y$ = 100 MPa, $C_1$ = 400000 MPa, $\gamma_1$ = 8000 MPa, $C_2$ = 400000 MPa, $\gamma_2$ = 4000, $C_3$ = 1240000 MPa, $\gamma_3$ = 2000, $C_4$ = 10000 MPa, $\gamma_4$ = 500, $C_5$ = 4200 MPa, $\gamma_5$ = 150, $C_6$ = 2200 MPa, $\gamma_6$ = 20 |
| Uniaxial ratcheting test | $\mu_i$ = 0.2 |

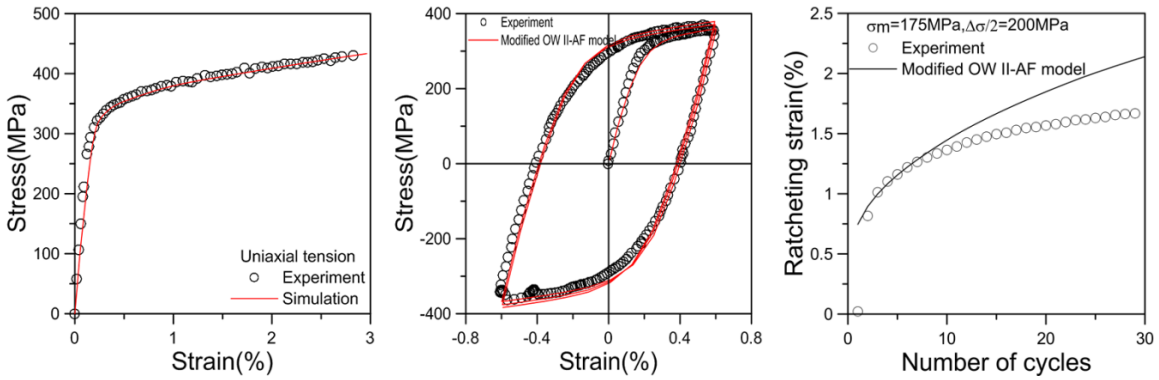


(a) Uniaxial tension (b) Hysteresis loop (c) Uniaixla ratcheting strain

Fig. 34 Parameter determination and simulation of hysteresis loop and uniaxial ratcheting effect by the modified model

agreement with experimental data in initial ten cycles, but later slgihtly larger. The parameters of the proposed model, which were determined by the references, were listed in Table 10.

### *5.1.12 Verification and Advantage of the proposed model*

The predicted results of AKO VI model were compared with those of MHAKO model, which indicated that the predicted resuslts of MHAKO model with the cyclic hardening function $\varphi(p)$

were smaller than those of AKO VI model, as given in Fig. 35.

The predicted results of OW II-AF model were compared with those of the modified OW II-AF model, which indicated that the predicted resuslts of the modified OW II-AF model with the cyclic hardening function $\varphi(p)$ were smaller than those of OW II-AF model, as given in Fig. 36.

Table 10 The material parameters of the modified model

| Test type | Parameters |
|---|---|
| Uniaxla tension | $\sigma_y$ = 100 MPa, $C_1$ = 320000 MPa, $\gamma_1$ = 8000 MPa, $C_2$ = 400000 MPa, $\gamma_2$ = 4000, $C_3$ = 1240000 MPa, $\gamma_3$ = 2000, $C_4$ = 10000 MPa, $\gamma_4$ = 500, $C_5$ = 4200 MPa, $\gamma_5$ = 150, $C_6$ = 2200 MPa, $\gamma_6$ = 20 |
| Uniaxial/Multiaxial test | $\eta_0$ = 0.3, $\omega$ = 1.0, $\eta_\infty$ = 0.3, $\chi$ = 3 |
| Cyclic hardneing parameter | $\varphi_\infty$ = 0.8, $\omega_\varphi$ = 15 |

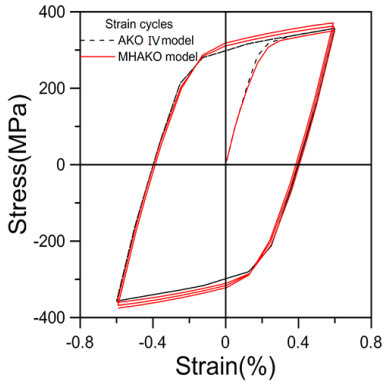


(a) Hysteresis loop

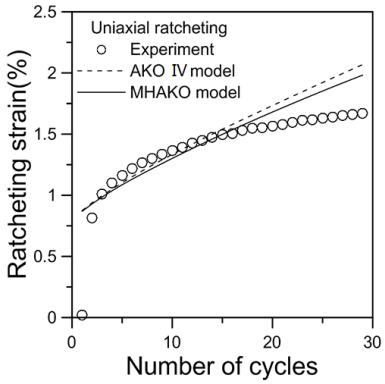


(b) Uniaixla ratcheting strain

Fig. 35 Comparison of hysteresis loop and uniaxial ratcheting effect by AKO IV model and MHAKO model

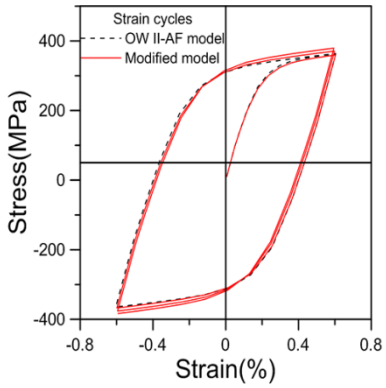


(a) Hysteresis loop

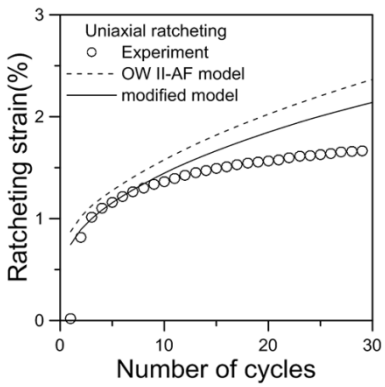


(b) Uniaixla ratcheting strain

Fig. 36 Comparison of hysteresis loop and uniaxial ratcheting effect by OW II-AF model and modified model

(a) (b)

Fig. 37 EPFEA model of Pressurized curved pipe under symmetric cyclic bending: (a) meshing; and (b) Load and constrain

### *5.2 Comparison of shell element and solid element*

The elbow specimen and loading prescribed was doubly symmetric, so only one quarter of the specimen was prescribed for force-controlled experimental simulations. Consequently, only half of the force was prescribed for force-controlled experimental simulations. The boundary conditions of the model came from the double symmetry of specimen and loading in addition. Internal pressure was applied to the structure inner surface and the reversed bending load in $y$ direction was imposed at the central point of the pipe end. Hence, the elbow was modeled with Solid45 elements in ANSYS. The finite element mesh, load and constrains were presented in Fig. 37. Non-linear geometry was also considered in the analysis.

Fig. 38 showed the comparison of predicted results of elbow pipe with real dimension and equal wall thickness with solid elements and experimental results. The hoop ratcheting strains of the elbow at 0° and 90° positions were shown in Fig. 38. It revealed the ratcheting strains of the elbow pipe with equal wall thickness were larger than those of the elbow pipe with real dimension at the outside surface of elbow pipes. Moreover, it also revealed that the predicted results of elbow pipe with the equal wall thickness were relatively more conservative than those of elbow pipe with the real dimension under outside surface of elbow pipes. Ratcheting strains distribution of elbow

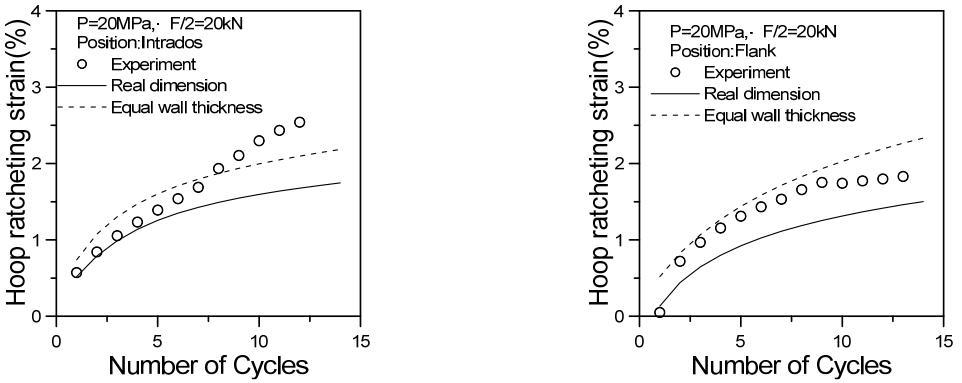


(a) At intrados (b) At flank

Fig. 38 Comparison of the prediction results and experimental results

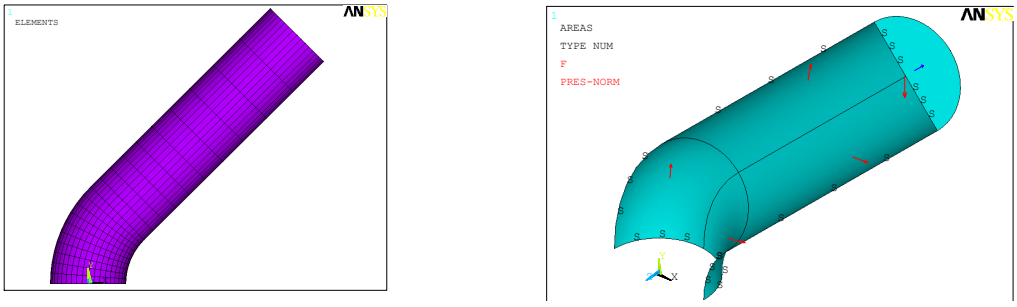


(a) Mesh (b) Constrains and loads

Fig. 39 Finite element model: (a) Mesh; (b) Constrains and loads

pipe corresponded to the change of standard elbow wall thickness during manufacturing process, which satisfied Chinese Code GB12559-90. The maximum difference of ratcheting strain was approximal 50%. Further, it was over conservative that real dimension was replaced by the equal wall thickness. However, the predicted results of the equal wall thickness instead of real dimension were over prediction, which was also one reason of unreasonable prediction results of other constitutive models. Moreover, the predicted results of elbow with equal wall thickness were more slightly over prediction than those of elbow with real dimension. Thus, the ratcheting strains of elbow were influenced by wall thickness.

In addition, the elbow can be considered as thin shell structure. The elbow pipe was modeled with Shell181 elements in ANSYS. The finite element mesh, load and constrains were presented in Fig. 39.

The force-controlled test was conducted, the first step of 12SER1, with the bending load of 20 kN and internal pressures of 17.5 MPa. Fig. 40 showed a typical distribution of ratcheting strain with the Chaboche model after 10 cycles, respectively. It can be seen from Fig. 40 that the biggest ratcheting strains occured at 45°positions of outside surfaces. And there were also ratcheting strains at flanks. Ratcheting strain regions of outside surface, the centers of which were thought as the flank of *xz* symmetry plane and the 45° position between intrados and flank respectively, extended along the meridional and circumferential direction.

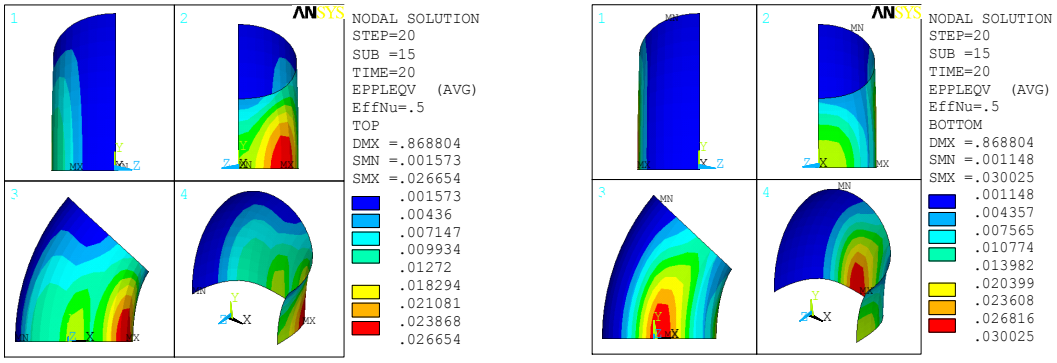


(a) Outside (b) Inside

Fig. 40 Equivalent plastic strain with Chaboche model

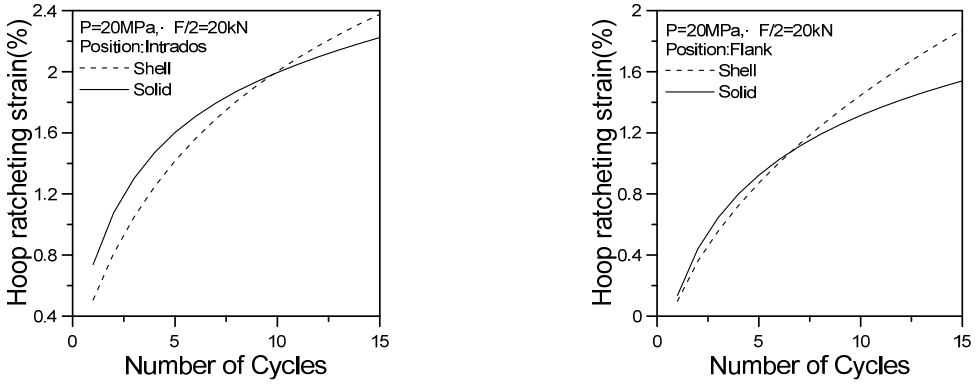


(a) At intrados (b) At flank

Fig. 41 Comparison of the prediction results using shell element and solid element

The equal wall thickness of elbow pipe with both shell and solid element models, which were simulated by Chaboche model. The simulation results were shown in Fig. 41. Compared the simulated results of both shell and solid element model, it found that the simulated results of shell elements were slightly bigger than those of solid elements. The maximum difference of ratcheting strains was approximal 20%. It was reasonable because shell elements were more conservative than solid elements. The ratcheting strains of the elbow pipe with equal wall thickness using solid elements were larger than those of the elbow pipe with real dimension under outside surface of elbow pipes. Thus, the ratcheting strains of the elbow pipe with equal wall thickness using shell elements were larger than those of the elbow pipe with real dimension under outside surface of elbow pipes. The shell elements instead of solid elements were feasible.

### *5.3 Simulations with ANSYS-bilinear, multilinear, AF and Chaboche models*

#### *5.3.1 Linear kinematic model*

Fig. 42 showed the comparison of ratcheting strain of elbow piping under internal pressure of 17.5 MPa and bending loading of 15 kN at flank. It was found that prediction results of BKH

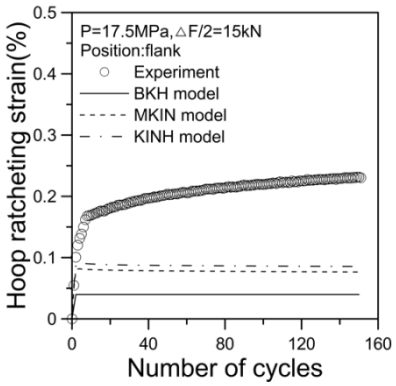


Fig. 42 Simulation of ratcheting strain of elbow pipe by BKH, MKIN/KINH model

model, MKIN model and KINH model underpredicted experimental data, and shakedown state appeared.

### *5.3.2 Armstrong-Frederic model and Chaboche model*

The predicted ratcheting behavior of elbow piping with AF model, CH3 model and CH4 model were compared with experimental data, as shown in Fig. 43. The predicted results of AF model were the lowest. It was found that the predicted results of CH4 model were smaller than those of CH3 model. Ratcheitng strain was simulated by CH3 model and CH4 model with and without isotropic hardening rule. It was found that the predicted results of CH3 model and CH4 model with isotropic hardening rule were smaller than those of CH3 model and CH4 model without isotropic hardening rule.

### *5.3.4 Ohno-Wang and modified Ohno-Wang models*

#### *5.3.3.1 OW I model*

The predicted ratcheting strain of elbow piping using OW I model under internal pressure of 17.5 MPa and bending loading of 15 kN was compared with experiemental data at flank, as given in Fig. 44. It was obversed that the predicted results of OW I model were smaller than experiemental data.

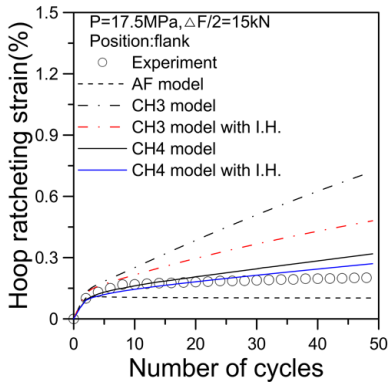


Fig. 43 Simulation of ratcheting strain of elbow pipe by AF, CH3 and CH4 model

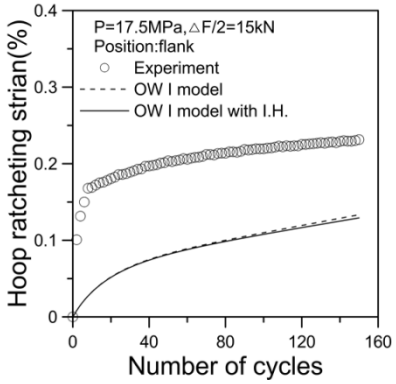


Fig. 44 Simulation of ratcheting strain of elbow pipe by OW I model

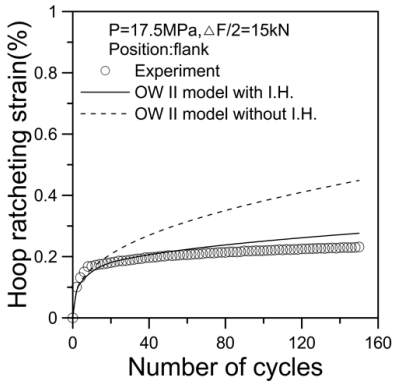


Fig. 45 Simulation of ratcheting strain of elbow pipe by OW II model

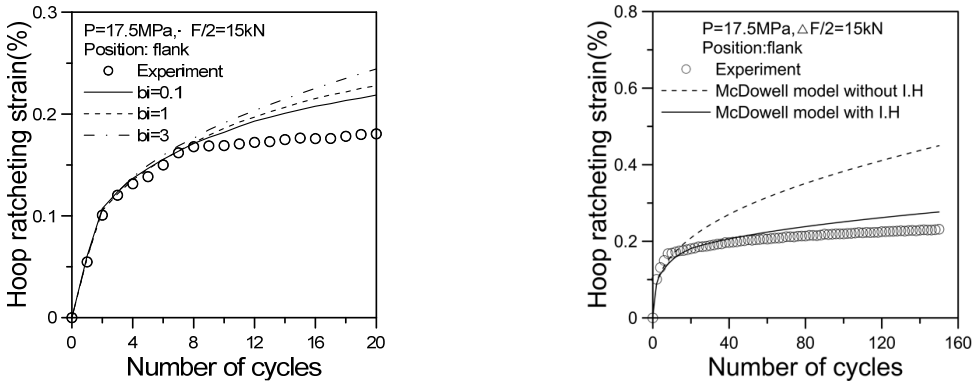


Fig. 46 Simulation of ratcheting strain of elbow pipe by Mc model

#### *5.3.3.2 OW II model*

Fig. 45 gave that the predicted ratcheting strain of elbow piping using OW II model with and without isotropic hardening rule under internal pressure of 17.5 MPa and bending loading of 15 kN was compared with experiemental data at flank. It was indicated that the predicted results of OW II model with isotropic hardening rule were in well agreement with experiemental data.

#### *5.3.3.3 Mc model*

Multiaxial ratcheting $b_i$ parameters were determined by elbow piping test, as shown in Fig. 46(a). It was seen from Fig. 46(a) that ratcheting strain increased with the increasing of the multiaxial parameter $b_i$. The predicted ratcheting strain of elbow piping using Mc model ($b_i$ = 1) with and without isotropic hardening rule under internal pressure of 17.5 MPa and bending loading of 15 kN was compared with experiemental data at flank, as given in Fig. 46. It was obversed that the predicted results of Mc model with isotropic hardening rule had good coherence to the experiemental data.

#### *5.3.3.4 JS and MJS model*

Fig. 47 showed that the predicted ratcheting strain of elbow piping using JS model with and

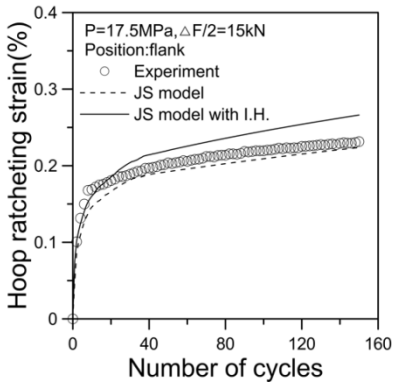


Fig. 47 Simulation of ratcheting strain of elbow pipe by JS model

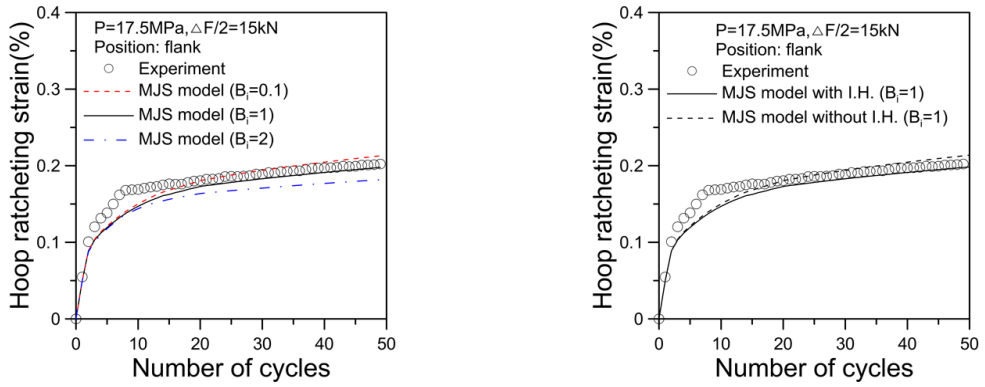


(a) (b)

Fig. 48 Ratcheting simulation of elbow piping by MJS model

without isotropic hardening rule under internal pressure of 17.5 MPa and bending loading of 15 kN was compared with experiemental data at flank. It was indicated that the predicted results of JS model with isotropic hardening rule had good consistency with experiemental data.

Multiaxial ratcheting $B_i$ parameters were determined by elbow piping test, as shown in Fig. 48(a). It was seen from Fig. 48(a) that ratcheting strain increased with the increasing of the multiaxial parameter $B_i$. The predicted ratcheting strain of elbow piping using MJS model with and without isotropic hardening rule under internal pressure of 17.5 MPa and bending loading of 15 kN was compared with experiemental data at flank, as given in Fig. 48(b). It was obversed that the predicted results of MJS model with isotropic hardening rule were in well agreement with experiemental data.

#### *5.3.3.5 CJK model*

It was seen from Fig. 49(a) that ratcheting strain decreased with the increasing of the multiaxial parameter $\chi_i$. Fig. 49(b) gave multiaxial ratcheting $\chi_i$ =0.01 parameter determination by means of elbow piping test. The predicted ratcheting strain of elbow piping using CJK model with and without isotropic hardening rule under internal pressure of 17.5 MPa and bending loading of 15

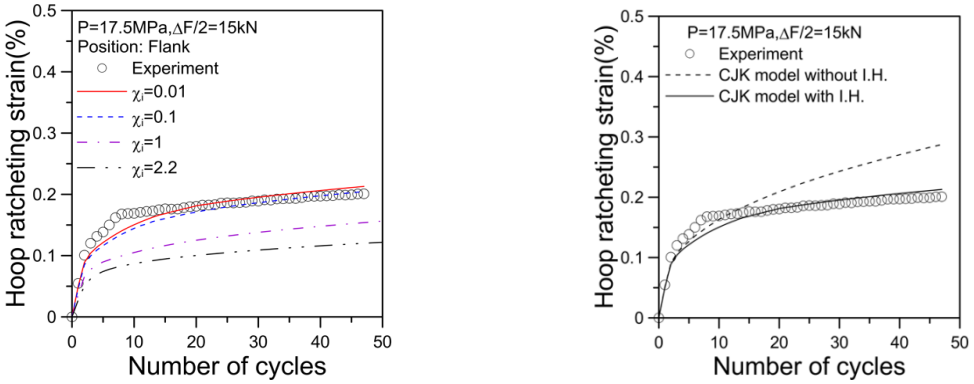


(a) (b)

Fig. 49 Simulation of ratcheting strain of elbow pipe by CJK model

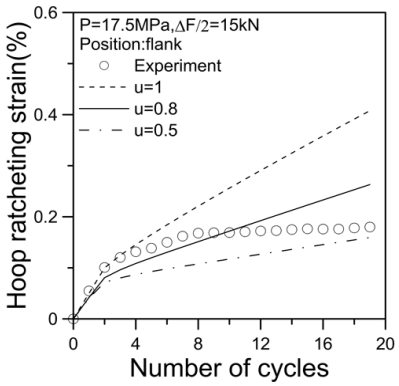


Fig. 50 Ratcheting simulation for elbow piping by Abdel Karim-Ohno model

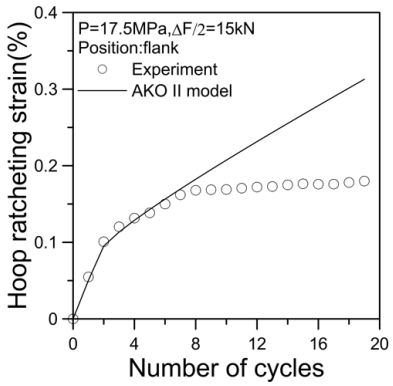


Fig. 51 Ratcheting simulation for elbow piping by AKO II model

kN was compared with experiemental data at flank. It was obversed that the predicted results of CJK model with isotropic hardening rule had good coherence to the experiemental data.

### *5.3.4 Abdel Karim-Ohno and modified Abdel Karim-Ohno models*

#### *5.3.4.1 Const $u_i$*

The parameter $\mu$ = 0.8 was determined by elbow piping test under internal pressure of 17.5 MPa and bending loading of 15 kN, as shown in Fig. 50. It was seen from Fig. 50 that ratcheting strain increased with the increasing number of cycles.

#### *5.3.4.2 Divided from η*

Fig. 51 gave that ratcheting strain of elbow piping under internal pressure of 17.5 MPa and bending loading of 15 kN increased with the increasing of number of cycles. It was found that ratcheting strain using modified AbdelKarim-Ohno model in initial cycles was in well agreement with experiemental data at flank. Comparison of Figs. 50 and 51, which indicated that the parameter $\eta$ was divided to the benefit of the improved predicted results.

#### *5.3.4.3 OW I-AF model*

Fig. 52 gave that the experiemental data of elbow piping at flank was compared with the predicted ratcheting strain using OW I-AF model under internal pressure of 17.5 MPa and bending loading of 15 kN. It was obversed that the experiemental data and predicted results of OW I-AF model (AKO IV) in intial cycles were the closest.

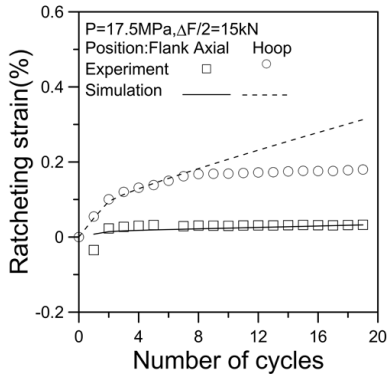


Fig. 52 Simulation of ratcheting strain of elbow pipe by AKO IV modeld

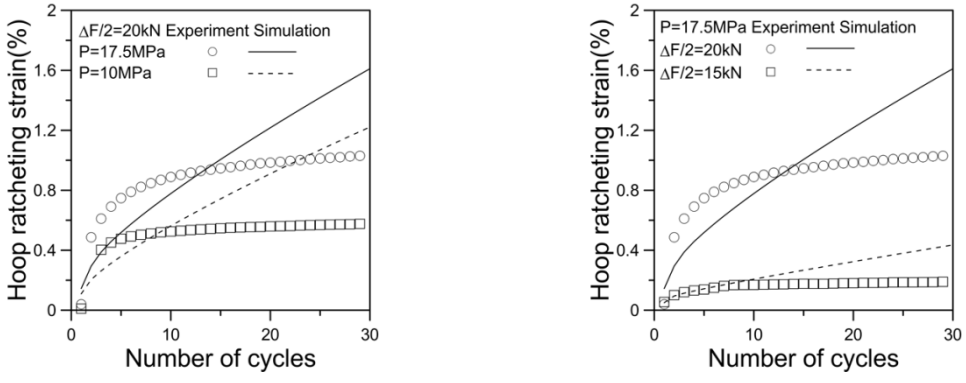


Fig. 53 Simulation of ratcheting strain of elbow pipe by AKO IV model

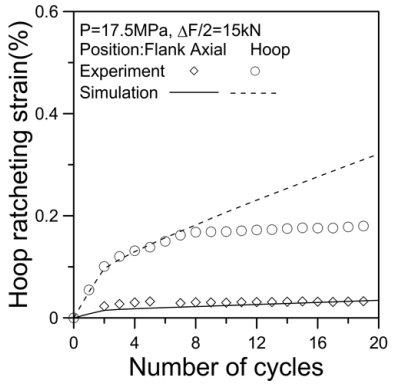


Fig. 54 Simulation of ratcheting strain of elbow pipe by modified OW I-AF model (MHAKO)

The effect of internal pressure under the same cyclic bending loading on ratcheting strain was given in Fig. 53(a). It was observed that the ratcheting strain rate increased with the increasing of inner pressure under the same bending loading. Fig. 53(b) showed the effect of cyclic bending loading under the same internal pressure on ratcheting strain. It was shown that the ratcheting strain rate increased with the increasing of a bending loading under the same inner pressure.

#### *5.3.4.4 Modified OW I-AF model*

The experiemental data of elbow piping at flank under internal pressure of 17.5 MPa and bending loading of 15 kN was compared with the predicted ratcheting strain using the modified OW I-AF model. It was found in Fig. 54 that the predicted results of the modified OW I-AF model in intial cycles were in well agreement with experiemental data. The predicted result was larger than foregoing results with the increasing of number of cycles.

### *5.3.5 OW II-AF model*

Fig. 55 indicated the predicted ratcheting strain of elbow piping using OW II-AF model under internal pressure of 17.5 MPa and bending loading of 15 kN was compared with experiemental data at flank. It was obversed that the predicted results of OW II-AF model were in well agreement

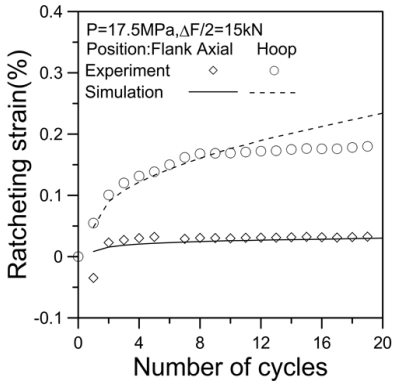


Fig. 55 Simulation of ratcheting strain of elbow pipe by OW II-AF model

with experiemental data. Comparison of a series of OW I-AF models with OW II-AF model, which indicated that the predicted results of OW II-AF model were better than those of a series of OW I-AF models. Because the leap function $H(f_i)$ of OW I-AF model was replaced by the nonlinear term $\left(\frac{\overline{\alpha}_i}{r_i}\right)^{m_i}$ of OW II-AF model.

### *5.3.6 Modified OW II-AF model*

Elbow piping was subjected to internal pressure of 17.5 MPa and bending loading of 15 kN. Comparison of the predicted ratcheting strain using the modified OW II-AF model with experiemental data at flank, as given in Fig. 56. It was shown in Fig. 56 that the predicted results of he modified OW II-AF model had good coherence to the experiemental data.

### *5.4 Simulation ratcheting behavior of elbow piping using CJK model*

Comparison of ratcheting strain of elbow pipe under internal pressure of 17.5 MPa and bending load of 15 kN and 20 kN respectively was shown in Fig. 57(a). It showed that ratcheting strain rate

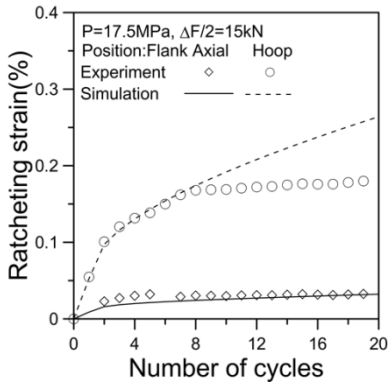


Fig. 56 Simulation of ratcheting strain of elbow pipe by the modified OW II-AF model

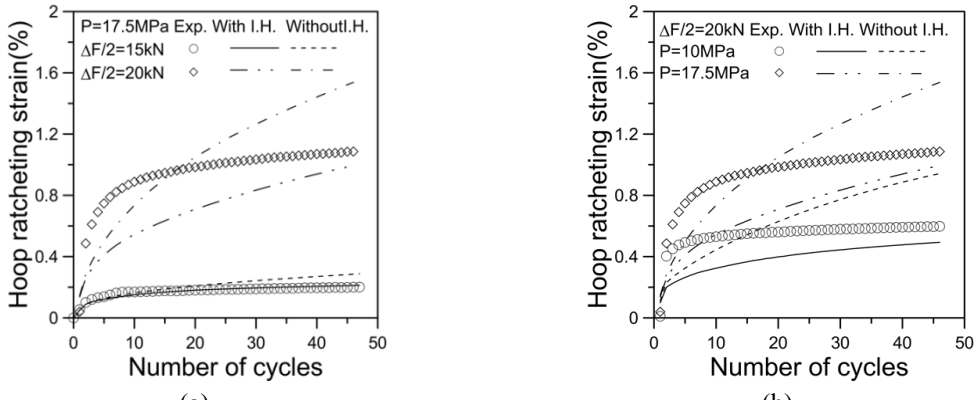


Fig. 57 Ratcheting simulation by CJK model under different internal pressures or bending load

increased with increasing of bending load under the same internal pressure. Fig. 57(b) gave comparison of ratcheting strain of elbow pipe under bending load of 20 kN and internal pressure of 10 MPa and 17.5 MPa respectively. Under the same bending load the ratcheting strain rate increased with increasing of internal pressure as shown in Fig. 57(b).

Fig. 58 gave the comparison of hoop ratcheting strain predicted by CJK model with and without isotropic hardening rule. It was observed that this model with isotropic hardening rule agreed well with the experimental data of 12SER4. The predicted hoop ratcheting strain by CJK model was compared with experimental data of 12SER1 and 12SER3. It was shown that this model without isotropic hardening rule overpredicted the experimental data. However, The CJK model with isotropic hardening rule predicted the experimental data well. It was observed that the predicted results of CJK model with isotropic hardening rule were slightly better than those without isotropic hardening rule, which was attributed to the effect of isotropic hardening. The CJK model without isotropic hardening rule cannot reflect the cyclic hardening behavior for strain controlled cycling, thus, the incorporation of isotropic hardening into the CJK model was

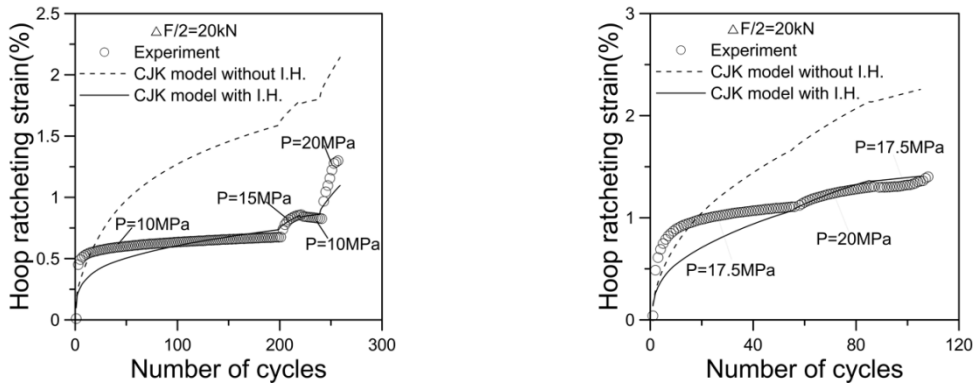


(a) 12SER3 (b) 12SER1

Fig. 58 Ratcheting simulation by CJK model under multi-step loadings

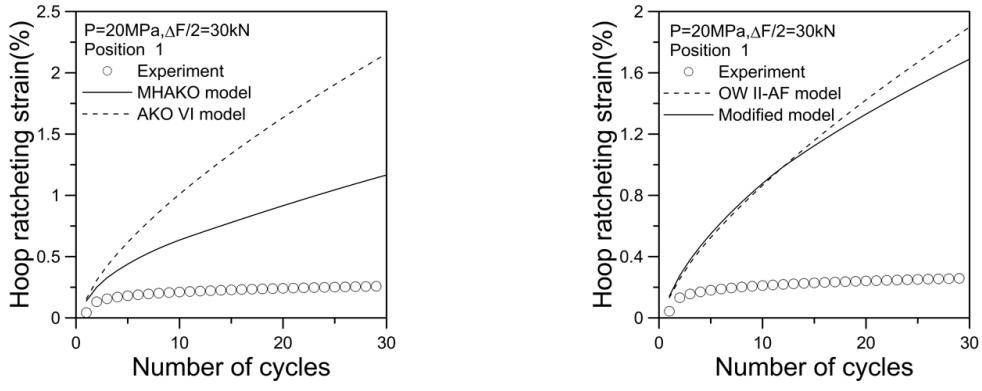


(a) (b)

Fig. 59 Comparison of ratcheting effect of straight pipe by AKO VI model and MHAKO model with and without cyclic hardening

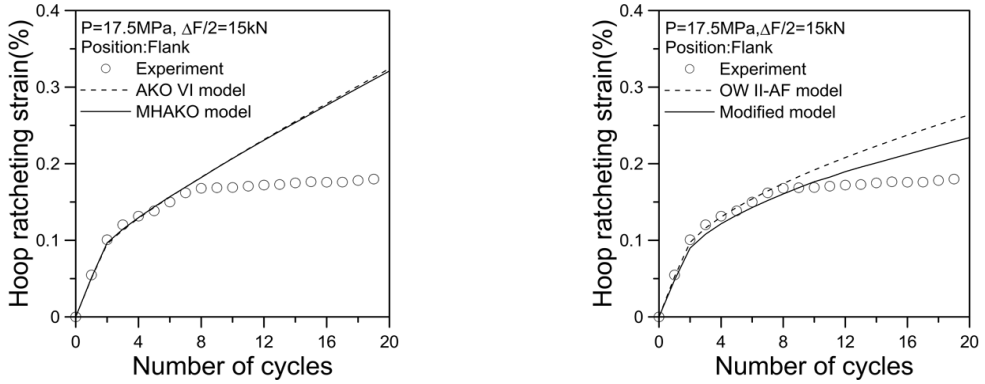


Fig. 60 Comparison of ratcheting effect of elbow piping by OW II-AF model and modified model with and without cyclic hardening

necessary. In addition, it was shown in Fig. 59 that the difference of ratcheting strain between the two cases increased with the number of cycles, which was due to the fact that CJK model with isotropic hardening continue to harden during cyclic loading.

### *5.5 Simulation ratcheting behavior of elbow piping using modified OW II-AF model*

The predicted results of strain cycling and uniaxial ratcheting strain for OW I-AF model and modified OW I-AF with cyclic hardening function were shown in Fig. 59. Fig. 60 gave OW II-AF model and modified OW II-AF with cyclic hardening function. It was found that ratcheting strain was affected by cyclic hardening characteristic. It verified the high reliability of the proposed model.

## 6. Conclusions

The paper described the ratcheting strains of pressurized elbow pipe under in-plane cyclic bending based upon experiment and finite element analysis. It can be conculded from the paper as follow:

(1) Ratcheting strain occurred mainly in the hoop direction and the maximum ratcheting strain occurred mainly at flanks or intrados. The ratcheting strain rate increased with the increase of internal pressure under the same bending loading or with the increase of the bending loading at the same internal pressure.

(2) Both shell element and solid element with real dimension and the equal wall thickness were compared by the finite element analysis. Results indicated that the ratcheting strains of pressurized elbow piping under reversed bending did correspond to the real dimension. Compared shell elements with solid elements, for elbow with the equal wall thickness, which showed that the ratcheting strains of elbow with shell elements were slightly larger than those of elbow with the solid elements. The ratcheting strain of elbow pipes was not only attributed to the wall thickness of elbow pipe, but also the influence of element types.

(3) The AF type models both with the presence and absence of isotropic hardening rule were implemented into ANSYS software. The ratcheting strain of pressurized elbow pipe under

in-plane reversed bending was simulated by elastic-plastic finite element analysis. Experimental data was compared with the predicted values of AF type models with and without isotropic hardening rule. It was observed that the predicted ratcheting strains by AF type models model with isotropic hardening rule were slightly better than those without isotropic hardening rule. Results indicated that isotropic hardening rule influenced on ratcheting behavior of elbow piping. In other words, it was shown that AF type models with isotropic hardening rule simulated the experimental data well. CJK model in all AF type models was the best model which was used to simulate ratcheting behavior of pressurzied elbow piping under in-plane reversed bending.

(4) Dynamic strain aging of austenitic stainless steel Z2CND18.12N was observed by means of unaixal tension test with different strain rate. Therefore, a modified OW II-AF model, which contained cycle hardening/softening characteristics, was proposed in the paper.

## Acknowledgments

The authors gratefully acknowledge financial support for this work from the Youth Foundation of Hebei Educational committee (No. QN2015336), Fundamental Research Funds for the Central Universities (XNB2015001), Central University Basic Scientific Research Business Expenses (No. L1523001) and National Natural Science Foundation of China (No. 51435012, 51475086).

## References

Abdel-Karim, M. and Ohno, N. (2000), "Kinematic hardening model suitable for ratchetting with steady-state", *Int. J. Plast.*, **16**(3-4), 225-240.

ANSYS, Inc. (2004), Guide to ANSYS user programmable Features (ANSYS release 9.0).

Armstrong, P. and Frederick, C. (1966), "A mathematical representation of the multiaxial bauchinger effect", CEGB Report No RD/BN 731.

Asada, S., Yamashita, N., Okamoto, A. and Nishiguchi, I. (2002), "Verification of alternative criteria for shakedown evaluation using flat head vessel", *Proceedings of the Pressure Vessels and Piping Conference*, Vancouver, BC, Canada, August, pp. 17-23.

ASME (2007), American society of mechanical engineers, Section III, New York, NY, USA.

Bari, S. and Hassan, T. (2000), "Anatomy of coupled constitutive models for ratcheting simulation", *Int. J. Plast.*, **16**(3-4), 381-409.

Bari, S. and Hassan, T. (2002), "An advancement in cyclic plasticity modeling for multiaxial ratcheting simulation", *Int. J. Plast.*, **18**(7), 873-894.

Benallal, A. and Marquis, D. (1987), "Constitutive equations for nonproportional cyclic elasto viscoplasticity", *J. Eng. Mater .Technol. ASME*, **109**(4), 326-336.

Besseling, J.F. (1958), "A theory of elastic, plastic and creep deformations of an initially isotropic material showing anisotropic strain-hardening, creep recovery, and secondary creep", *J. Appl. Mech.*, **25**, 529-536.

Boussaa, D., Labbe, P. and Tang, H. (1993), "Fatigue-ratcheting analysis of pressurized elbows", *ASME PVP*, **266**, 13-21.

Chaboche, J.L. (1986), "Time-independent constitutive theories for cyclic plasticity", *Int. J. Plast.*, **2**(2), 149-188.

Chaboche, J.L. (1991), "On some modifications of kinematic hardening to improve the description of ratchetting effects", *Int. J. Plast.*, **7**(7), 661-678.

Chaboche, J.L. and Dang, V. (1979), "Modelization of the strain memory effect on the cyclic hardening of 316 stainless steel", *Proceedings of the 5th International Conference on SmiRT*, *Div. L*, Berlin, Germany.

Chen, X. and Jiao, R. (2004), "Modified kinematic hardening rule for multiaxial ratcheting prediction", *Int. J. Plast.*, **20**(4-5), 871-898.

Chen, X.H. and Chen, X. (2015), "Study on ratcheting effect of pressurized straight pipe with local wall thinning using finite element analysis", *Proceedings of the 14th International Conference on Pressure Vessel Technology* (*ICPVT*), Shanghai, China, September, **Volumes 139-140**, pp. 69-76. DOI: 10.1016/j.ijpvp.2016.03.005

Chen, X.H. and Chen, X. (2016), "Effect of local wall thinning on ratcheting behavior of pressurized 90° elbow pipe under reversed bending using finite element analysis", *Steel Compos. Struct., Int. J.*, **20**(4), 931-950.

Chen, X., Gao, B. and Chen, G. (2005a), "Multiaxial ratcheting of pressurized elbows subjected to reversed in-plane bending", *J. Pres. Eq. Syst.*, **3**, 38-44.

Chen, X., Jiao, R. and Kim, K.S. (2005b), "On the Ohno–Wang kinematic hardening rules for multiaxial ratcheting modeling of medium carbon steel", *Int. J. Plast.*, **21**(1), 161-184.

Chen, X., Gao, B. and Chen, G. (2006), "Ratcheting study of pressurized elbows subjected to reversed in-plane bending", *J. Pres. Ves. – Trans. ASME*, **128**(4), 525-532.

Chen, X.H., Chen, X., Yu, D.J. and Gao, B.J. (2013), "Recent progresses in experimental investigation and finite element analysis of ratcheting in pressurized piping", *Int. J. Pres. Ves. Pip.*, **101**, 113-142.

Chen, X.H., Chen, X., Chen, G. and Li, D.M. (2015), "Ratcheting behavior of pressurized Z2CND18.12N stainless steel pipe under different control modes", *Steel Compos. Struct., Int. J.*, **18**(1), 29-50.

Chen, X.H., Chen, X., Yu, W.W. and Li, D.M. (2016), "Ratcheting behavior of pressurized 90° elbow piping subjected to reversed in-plane bending with a combined hardening model", *Int. J. Pres. Ves. Pip.*, **137**, 28-37.

DeGrassi, G., Hofmayer, C., Murphy, A., Suzuki, K. and Namita, Y. (2003), "BNL nonlinear pre-test seismic analysis for the NUPEC ultimate strength piping test program", *Trans SMiRT*, 17, BNL-NUREG-71119-2003-CP.

DeGrassi, G., Nie, J. and Hofmayer, C. (2008), "Seismic analysis of large-scale piping systems for the JNES/NUPEC ultimate strength piping test program", NUREG/CR-6983, US Nuclear Regulatory Commision, Washington, D.C., USA.

EN13445-3 (2002), Unfired Pressure Vessels-Part 3: Design, Annex C: Method based on stress categories.

Fenton, M. and Hassan, T. (2014), "Low-cycle fatigue failure responses of long and short radius elbows", *ASME PVP*, V008T08A024.

Gao, B. (2005), "Modeling of material multiaxial ratcheting and ratcheting prediction of pressure piping", Ph.D. Dissertation; Tianjin University of Technology, China. [In Chinese]

Gao, B., Chen, X. and Chen, G. (2006), "Ratchetting and ratchetting boundary study of pressurized straight low carbon steel pipe under reversed bending", *Int. J. Pres. Ves. Pip.*, **83**(2), 96-106.

Gaudin, C. and Feaugas, X. (2004), "Cyclic creep process in AISI 316L stainless steel in terms of dislocation patterns and internal stresses", *Acta Mater.*, **52**(10), 3097-3110.

Halama, R. (2008), "A modification of abdelkarim-ohno model for ratcheting simulations", *Technical Gazette*, **15**(3), 3-9.

Hassan, T. and Rahman, S.M. (2009), "Simulation of ratcheting responses of elbow piping components", *Proceedings of the Pressure Vessels and Piping Conference*, Prague, Czech Republic, July, pp. 103-108.

Hassan, T. and Rahman, M. (2015), "Constitutive models in simulating low-cycle fatigue and ratcheting responses of elbow", *J. Pres. Ves. – Trans. ASME*, **137**(3), 031002-1-12.

Hassan, T., Rahman, M. and Bari, S. (2015), "Low-cycle fatigue and ratcheting responses of elbow piping components", *J. Pres. Ves. – Trans. ASME*, **137**(3), 031010-1-12.

Huang, C.T., Iwan, W., Jaquay, K. and Chokshi, N. (1998), "Cyclic moment response characteristics and seismic margins of elbows", *ASME PVP*, **360**, 271-282.

Jiang, Y.Y. and Sehitoglu, H. (1996), "Modeling of cyclic ratcheting plasticity, part I: development of constitutive relations", *J. Pres. Ves. – Trans. ASME*, **63**(3), 720-725.

Jiang, Y.Y. and Sehitoglu, H. (1996), "Modeling of cyclic ratcheting plasticity, part II: comparison of model simulations with experiments", *J. Pres. Ves. – Trans. ASME*, **63**(3), 726-733.

KTA (1995), Kerntechnischer Ausschuß; Sicherheitstechnische Regel des KTA, Komponenten des primärkreises von Leichtisserreaktoren, Teil: Auslegung, Konstruktion und Berchnung, Regeländerungsentwurf.

Kang, G.Z., Gao, Q. and Yang, X.J. (2004), "Uniaxial and non-proportionally multiaxial ratcheting of SS304 stainless steel at elevated temperature: Experiments and simulations", *Int. J. Nonlinear Mech.*, **39**(5), 843-857.

Marquis, D. (1979), "Modélisation et identification de l'écrouissage anisotrope des métaux", Thése de 3éme cycle; Université Paris 6, France.

McDowell, D. (1995), "Stress state dependence of cyclic ratchetting behavior of two rail steels", *Int. J. Plast.*, **11**(4), 397-421.

McDowell, D. (1997), "An approximate algorithm for elastic-plastic two-dimensional rolling/sliding contact", *Wear*, **211**(2), 237-246.

Moreton, D., Yahiaoui, K. and Moffat, D. (1996), "Onset of ratchetting in pressurised piping elbows subjected to in-plane bending moments", *Int. J. Pres. Ves. Pip.*, **68**(1), 73-79.

Ohno, N. and Wang, J.D. (1993a), "Kinematic hardening rules with critical state of dynamic recovery, part I: formulation and basic features for ratchetting behavior", *Int. J. Plast.*, **9**(3), 375-390.

Ohno, N. and Wang, J.D. (1993b), "Kinematic hardening rules with critical state of dynamic recovery. Part II: Application to experiments of ratcheting behavior", *Int. J. Plast.*, **9**(3), 391-403.

Owen, D., Prakash, A. and Zienkiewicz, O. (1974), "Finite element analysis of non-linear composite materials by use of overlay systems", *Comp. Struct.*, **4**(6), 1251-1267.

Prager, W. (1956), "A new method of analyzing stresses and strains in work-hardening plastic solids", *J. Appl. Math.*, **23**, 493-496.

R5 (1990), Assessment Procedure for the High Temperature Response of Structures, Nuclear Electric plc, **2**.

Rahman, S.M. (2006), "Finite element analysis and related numerical schemes for ratcheting simulation", Ph.D. Dissertation; North Carolina State University, Raleigh, NC, USA.

RCC-MR (1985), Design rules for class 1 equipment, RCC-MR codes; Revision.

Rojíčeka, J. and Halama, R. (2008), "Numerical simulations of pipeline bending tests", *Appl. Comp. Mech.*, **2**(1), 347-356.

Stearns, J.C., Lam, P.C. and Scavuzzo, R.J. (1993), "Incremental plastic strain of a pipe elbow with varying bend radii", *Proceedings of the Pressure Vessels and Piping Conference*, Denver, CO, USA, July, pp. 169-174.

Touboul, F., Lacire, M., Blay, N., Blanchard, M. and Le Breton, F. (1998), "Simplified methods for the evaluation of the seismic behaviour of piping system for criteria application", *ASME PVP*, **364**, 117-128.

Varelis, G.E., Karamanos, S.A. and Gresnigt, A.M. (2013), "Pipe elbows under strong cyclic loading", *J. Pres. Ves. – Trans. ASME*, **135**(1), 011207-1-9.

Varelis, G.E. and Karamanos, S.A. (2014), "Low-cycle fatigue of pressurized steel elbows under in-plane bending", *J. Pres. Ves. – Trans. ASME*, **137**(1), 011401-1-10.

Vishnuvardhana, S., Raghavaa, G., Gandhia, P., Saravanana, M., Goyal, S., Arora, P., Guptab, S.K. and Bhasin, V. (2013), "Ratcheting failure of pressurised straight pipes and elbows under reversed bending", *Int. J. Pres. Ves. Pip.*, **105-106**, 79-89.

Wang, L., Chen, G., Zhu, J.B., Sun, X.H., Mei, Y.H., Ling, X. and Chen, X. (2015), "Bending ratcheting behavior of pressurized straight Z2CND18.12N stainless steel pipe", *Struct. Eng. Mech., Int. J.*, **52**(6), 1135-1156.

Yahiaoui, K., Moffat, D. and Moreton, D. (1996a), "Damage assessment of piping elbows loaded by steady internal pressure and dynamic in-plane or out-of-plane bending", *Proceedings of the International Conference on Pressure Vessel Technology ICPVT*, Volume 1, Montréal, QC, Canada, July, pp. 361-375.

Yahiaoui, K., Moffat, D. and Moreton, D. (1996b), "Pressurized piping elbows under simulated seismic bending: design code implications", *Proc. Inst. Mech. Eng. E.-J. Pro.*, **210**(3), 159-170.

Yamamoto, Y., Yamashita, N. and Tanaka, M. (2002), "Evaluation of thermal stress ratchet in plastic FEA", *Proceedings of Pressure Vessels and Piping Conference*, Vancouver, BC, Canada, August, pp. 3-10.

Zakavi, S.J. and Nourbakhsh, M. (2014), "The ratcheting behaviour of stainless steel pressurized piping

elbows subjected to dynamic out-of-plane moments", *Mod. Mech. Eng.*, **4**(3), 125-132.
Zakavi, S.J. and Rahmani, V. (2014), "The ratcheting rate of stainless steel pressurized piping branch under seismic loading", *Indian J. Sci. Res.*, **3**(1), 191-199.
Zakavi, S.J., Ajri, M. and Golshan, V. (2014), "The ratcheting behaviour of plain carbon steel pressurized piping elbows subjected to simulated seismic in-plane bending", *World J. Mech.*, **4**(7), 238-246.
Zhang, J. (2002), "Constitutive description for non-proportionally ratcheting of cyclically hardening material and its finite element implementation at high temperatures", Ph.D. Dissertation; Southwest Jiaotong University, China.

*CC*